



Numerical study on hydrodynamic effect of flexibility in a self-propelled plunging foil

Xiaojue Zhu, Guowei He, Xing Zhang*

The State Key Laboratory of Nonlinear Mechanics (LNM), Institute of Mechanics, Chinese Academy of Sciences, Beijing 100190, China



ARTICLE INFO

Article history:

Received 15 October 2013

Received in revised form 17 February 2014

Accepted 31 March 2014

Available online 13 April 2014

Keywords:

Fluid–structure interaction

Passive flexibility

Self-propulsion

Plunging foil

Immersed boundary method

Vortex street

ABSTRACT

The present study is a numerical investigation of the hydrodynamic effects of passive flexibility on a self-propelled plunging foil. In the model problem, the flow is two-dimensional, incompressible and laminar, while the flexible foil is treated as an inextensible filament. The leading-edge of the foil undergoes a prescribed harmonic oscillation in the vertical direction. In the horizontal direction, the foil is free to move and no constraint is imposed. The simulations are performed by using a solver which couples the immersed boundary method for the flow and the finite difference method for the structure. A systematic parametric study has been conducted to investigate the effects of flexibility on important physical quantities such as the cruising speed, swimming power and propulsive efficiency. It is found that optimal cruising speed is always achieved in foils with some passive flexibility and not the rigid ones. Another important finding is that optimum performance is always achieved at a forcing frequency much lower than the resonance point. Based on the simulation results, three dynamical states of a self-propelled foil have been identified with the increase of bending rigidity, i.e., non-periodic movement, periodic backward-movement and periodic forward-movement. For a flexible foil in forward movement, depending on the range of bending rigidity, either a deflected or a symmetric vortex street arises as the characteristic wake structure. It is found that moderate flexibility is beneficial to symmetry preservation in the wake, while excessive flexibility can trigger symmetry-breaking. The results obtained in the current work shed some light on the role of flexibility in flapping-based biolocomotion.

© 2014 Elsevier Ltd. All rights reserved.

1. Introduction

Flapping motions of wings/fin are used by animals (such as birds, insects, bats and fishes) to generate lift or thrust to keep them aloft or propel themselves in the surrounding fluid. Researches in this area are not only motivated by the fundamental interest of understanding the mechanism of animal flight and swimming, but also the development of micro air vehicles (MAVs) and autonomous underwater vehicles (AUVs) based on biomimetics. A foil in steady forward motion and a combination of harmonic plunging and pitching has served as a simplified model for the study of efficient locomotion in animals. Till now extensive researches on flapping foils have been conducted, both experimentally and computationally.

Although (passive) flexibility of wing/fin has long been recognized as an important factor in the aerodynamic (hydrodynamic) performance of insect flight or fish swimming, it has received little

attention until recently (see [1,2] for a comprehensive review). By using a combination of computational and analytic methods, Daniel and Combes [3] have shown that the deformation in flapping wings was dominated less by aerodynamic loading than by inertial and elastic forces. In a series of experimental studies, chordwise and spanwise flexibility have been shown to increase propulsive efficiency in flapping-based propulsion [4–6]. In the works by Ishihara et al. [7] and Zhao et al. [8], a dynamically scaled mechanical model of flapping flight was used to measure the aerodynamic forces on flapping wings of variable flexural stiffness. Due to the complexity of fluid–structure interaction (FSI) problems, in computational simulations simplifications are usually made, either in the model for the fluid or for the structure. For example, Katz and Wehs [9] and Michelin and Llewellyn Smith [10] have used the potential flow theory to describe the interaction between an inviscid flow and a flexible flapping wing; whereas a reduced-order model has been used for the structures in other works [11–13]. With the availability of better computing power and more sophisticated numerical methods, simulations which include the interaction of viscous fluid and solid continuum were performed in some more recent studies [14–22].

* Corresponding author. Tel.: +86 10 82543929; fax: +86 10 82543977.

E-mail address: zhangx@lnm.imech.ac.cn (X. Zhang).

One point has to be underlined here: in most studies concerning flapping foils, the interaction between a flapping body held static and an oncoming flow driven independently is considered. However, the decoupling of the flapping dynamics and the forward speed makes those systems very dissimilar to free-flying (or free-swimming) animals. Thus the utilization of ‘self-propelled’ device is preferable in the study of biocomotion [23]. Till now, only limited studies have been conducted to understand the behaviors of ‘self-propelled’ flapping-foil systems. For rigid flapping foils, experimental studies on a model mounted on a ‘merry go round’ can be found in Vandenberghe et al. [24] and Vandenberghe et al. [25]; numerical simulations of simplified models can be found in Alben and Shelley [26], Lu and Liao [27], and Zhang et al. [28]. For flexible flapping foils, Spagnolie et al. [29] and Zhang et al. [30] used the ‘lumped-torsional’ model to mimic the flexibility of the structure (i.e., a plunging rigid plate with a torsion spring acting about the pivot at the leading edge to produce passive pitching). Eldredge and Pisani [31] and Wilson and Eldredge [32] have also performed simulations of a self-propelled flexible swimmers represented by an articulated system of linked rigid bodies. Recently, self-propelled flapping devices with realistic flexible wings were built to investigate the role of resonance in optimizing the performance [33, 34] and the scaling of cruising speed with foil length and bending rigidity [35]. A numerical study of such system was also performed in [35], where the foil is treated as an elastica and a ‘body-vortex-sheet’ model is used for the fluid. This fluid model is still based on the potential (inviscid) flow theory, although some empirical models were used to include the effect of viscous drag. Despite of the encouraging agreements between the experiments and the inviscid predictions, the range of validity of the inviscid assumption is still limited by the onset of dynamic stall. This is particularly true at low Reynolds numbers typically required in the flights of MAVs. Moreover, although some physical insights have been gained by using reduced-order models for the structures, the behavior of a dynamical system consisting of torsional springs and rigid components is still very different from that of an elastica. Thus we believe FSI simulations that use the Navier–Stokes equations for the fluid and the equation of solid continuum for the flexible foil are essential for elucidating the effect of flexibility on the performance of a self-propelled flapping system. We also noticed a most recent work by Lee and Lee [36], where numerical simulations of such system have been conducted by using the lattice Boltzmann method. Their work only focused on the effect of flexibility on propulsive velocity. To the best of our knowledge, a *thorough and systematic* study regarding the role of flexibility in such system still lacks in the literature.

In this paper, we proposed to model such system by considering the interaction of a self-propelled inextensible filament with a two-dimensional viscous flow. We developed a solver by coupling the Navier–Stokes equations for the fluid and a geometrically non-linear equation for the structure. The model problem is then systematically investigated by means of numerical simulations. The purposes of the current work are twofold. First, by using the data from the numerical simulations, we would like to clarify the speculation regarding the connection between performance optimum and occurrence of resonance. Second, we would like to uncover some information which are lacking in inviscid simulations or simulations using the ‘lumped-torsional’ model, e.g., the mode shape of the flexible foil during flapping and the true wake structure behind the foil in forward movement. Such information are crucial for understanding the role of flexibility in propulsive performance of a flapping-foil system.

The rest of the paper is arranged as follows. In Section 2, the model problem and governing equations are presented. In Section 3, the numerical methods and simulation set-up are described. Section 4 presents the results and discussions. Finally, some conclusions are drawn in Section 5.

2. Model problem and governing equations

We consider the model problem of a self-propelled flexible foil driven by the plunging motion (see Fig. 1). The foil is clamped at the leading-edge which undergoes a harmonic oscillation in the vertical direction, but is free to move horizontally.

The fluid flow is assumed to be laminar and incompressible. The governing equations are written in the dimensionless form as

$$\frac{\partial \mathbf{u}}{\partial t} + \nabla \cdot (\mathbf{u}\mathbf{u}) = -\nabla p + \frac{1}{Re_f} \nabla^2 \mathbf{u} + \mathbf{f}, \quad (1)$$

$$\nabla \cdot \mathbf{u} = 0, \quad (2)$$

where \mathbf{u} is the fluid velocity, p the pressure. Re_f is the flapping Reynolds number which is defined as $Re_f = \rho_f U_{ref} L / \mu$, with ρ_f , U_{ref} , L and μ being the density of fluid, reference velocity, chord length of the foil and dynamic viscosity of the fluid, respectively. \mathbf{f} is the (dimensionless) Eulerian forcing that is used to mimic the effect of the immersed object on the fluid flow. The reference velocity used in this work is $U_{ref} = 2\pi Af$, where f is the frequency of the plunging motion and A is the oscillation amplitude of the leading edge. Thus the reference velocity is equivalent to the maximum flapping velocity.

In this study, we consider a two-dimensional flow interacting with a flexible foil. Due to its small thickness-length-ratio, the flexible foil is treated as an inextensible filament. The governing equations for the motion of the filament can be written in a dimensionless form as

$$\beta \frac{\partial^2 \mathbf{X}}{\partial t^2} - \frac{\partial}{\partial s} \left(\zeta \frac{\partial \mathbf{X}}{\partial s} \right) + \frac{\partial^2}{\partial s^2} \left(\gamma \frac{\partial^2 \mathbf{X}}{\partial s^2} \right) = \beta Fr \frac{\mathbf{g}}{g} - \mathbf{F}, \quad (3)$$

$$\frac{\partial \mathbf{X}}{\partial s} \cdot \frac{\partial \mathbf{X}}{\partial s} = 1, \quad (4)$$

where s is the Lagrangian coordinate along the arc length; \mathbf{X} is the displacement vector; β , ζ and γ are the mass ratio, dimensionless tension coefficient and dimensionless bending rigidity respectively. \mathbf{F} is the (dimensionless) Lagrangian forcing term due to the interaction with the fluid; \mathbf{g} is the acceleration of gravity and $g = |\mathbf{g}|$. Fr is the Froude number defined as gL/U_{ref}^2 . The gravitational term in Eq. (3) is zero for all simulations performed in this paper except one validation case for the structural solver (see Section 3.2 for the details).

The dimensionless parameters, β , ζ and γ , are defined as

$$\begin{aligned} \beta &= \frac{\rho_s}{\rho_f L}, \\ \zeta &= \frac{T}{\rho_f U_{ref}^2 L}, \\ \gamma &= \frac{B}{\rho_f U_{ref}^2 L^3}, \end{aligned} \quad (5)$$

where ρ_s is the linear density of the filament; T and B are the dimensional tension and bending rigidity respectively. Eq. (3) is equivalent to those used by Zhu and Peskin [37], Connell and Yue [38] and Huang et al. [39] for flexible structures. Eq. (4) is the inextensibility condition which acts as a constraint on the

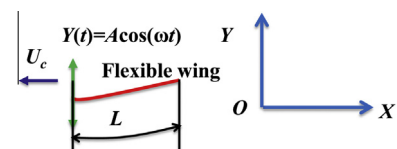


Fig. 1. Schematic depiction of the model problem: a self-propelled flexible foil of length L driven by a harmonic plunging motion at the leading-edge.

displacements of the structure. A Poisson equation for the tension coefficient $\zeta(s, t)$ can be derived from Eqs. (3) and (4) as

$$\frac{\partial \mathbf{X}}{\partial s} \cdot \frac{\partial^2}{\partial s^2} \left(\zeta \frac{\partial \mathbf{X}}{\partial s} \right) = \frac{1}{2} \frac{\partial^2}{\partial t^2} \left(\frac{\partial \mathbf{X}}{\partial s} \cdot \frac{\partial \mathbf{X}}{\partial s} \right) - \frac{\partial^2 \mathbf{X}}{\partial t \partial s} \cdot \frac{\partial^2 \mathbf{X}}{\partial t \partial s} - \frac{\partial \mathbf{X}}{\partial s} \cdot \frac{\partial}{\partial s} (\mathbf{F}_b - \mathbf{F}), \quad (6)$$

where $\mathbf{F}_b = -\frac{\partial^2}{\partial s^2} \left(\gamma \frac{\partial^2 \mathbf{X}}{\partial s^2} \right)$ is the bending force. The first term on the right hand side of Eq. (6) is zero theoretically. However, this term is kept to correct the numerical inextensibility errors introduced in the computation.

In the current study, there are some complications in the boundary conditions for Eqs. (3) and (6). For the leading-edge of a self-propelled flapping foil, its vertical (plunging) motion is prescribed as a harmonic function of time. By using L/U_{ref} as the reference parameter for time, the dimensionless form of this function becomes

$$y(t) = \bar{A} \cos \left(\frac{1}{\bar{A}} t \right), \quad (7)$$

where $\bar{A} = A/L$ is the dimensionless oscillation amplitude. The horizontal motion of the leading-edge is not constrained and the trailing-edge of the flapping foil is a free-end. The numerical issues including the implementation of boundary conditions for Eqs. (3) and (6) will be discussed in detail in Section 3.2.

3. Numerical methodology and simulation set up

3.1. Immersed-boundary flow solver

In this paper, the governing equation for fluid is numerically solved by using the immersed boundary technique, in which a body force is added to the momentum equation to mimic the effect of immersed objects on the flow. More specifically, we use a variant of the direct-forcing immersed boundary methods which is based on the discrete stream function formulation for incompressible Navier–Stokes equations [40].

The flexible foil placed in the flow is represented by a series of Lagrangian points (markers). The non-slip boundary condition to be imposed at the Lagrangian points is

$$\int_V \mathbf{u}(\mathbf{x}, t) \delta(\mathbf{x} - \mathbf{X}) d\mathbf{x} = \mathbf{U}_b(\mathbf{X}, t), \quad (8)$$

where δ is the regularized delta function (in this work, a 3-point regularized delta function is used [40]); \mathbf{U}_b is the desired velocity at the Lagrangian points. If the motion of the immersed body is prescribed, \mathbf{U}_b is known beforehand; while for FSI problems, \mathbf{U}_b is a priori unknown and must be obtained by solving the structural equation. The coupling between the flow solver and structural solver will be further discussed in Section 3.3.

To impose the boundary condition Eq. (8), a forcing term $\mathbf{F}(\mathbf{X}, t)$ is applied at the Lagrangian points. The forcing term $\mathbf{f}(\mathbf{x}, t)$ in Eq. (1) (which is applied at the computational grids or Eulerian points) is related to $\mathbf{F}(\mathbf{X}, t)$ by

$$\mathbf{f}(\mathbf{x}, t) = \int_S \mathbf{F}(\mathbf{X}(s), t) \delta(\mathbf{x} - \mathbf{X}(s)) ds. \quad (9)$$

To solve the Navier–Stokes equations, a transport equation for the discrete stream function is first derived from Eqs. (1) and (2). At every time step, the governing equation for the discrete stream function is then discretized and solved numerically. Comparing with the conventional projection method, this method is computationally more efficient. For the details of the numerical method, including the determination of forcing term $\mathbf{F}(\mathbf{X}, t)$, spatial discretization and time advancing scheme, please refer to [40]. Systematic validations of the flow solver on flows over stationary and moving

obstacles can also be found in [40], e.g., flows past a circular cylinder (at $Re = 40, 100, 200$), an in-line oscillating cylinder in fluid at rest, and flow past a three-dimensional low-aspect-ratio flat-plate of zero-thickness (at $Re = 100$). The predictions of lift, drag or velocity profiles were in excellent agreement with those from other literature.

3.2. Structural solver

A finite difference method on a staggered grid is used to solve the structural equations (Eqs. (3) and (6)). We largely follow the discretization and solution procedure proposed by Huang et al. [39], but make some modifications to the boundary conditions to allow free movement of the self-propelled foil in the horizontal direction.

The boundary conditions for Eqs. (3) and (6) are described as follows. At the trailing edge of the flapping foil, we use the free end condition:

$$\begin{aligned} \left(\frac{\partial^2 \mathbf{X}}{\partial s^2} \right)_{s=1} &= (0, 0), \\ \left(\frac{\partial^3 \mathbf{X}}{\partial s^3} \right)_{s=1} &= (0, 0), \\ \zeta_{s=1} &= 0. \end{aligned} \quad (10)$$

At the leading edge of the self-propelled foil, the vertical motion is prescribed and its orientation is strictly horizontal. The boundary conditions are then

$$\begin{aligned} (Y)_{s=0} &= y(t), \\ \left(\frac{\partial \mathbf{X}}{\partial s} \right)_{s=0} &= (1, 0), \\ \left(\frac{\partial^3 X}{\partial s^3} \right)_{s=0} &= 0, \\ \zeta_{s=0} &= 0, \end{aligned} \quad (11)$$

where X and Y are the horizontal and vertical components of the displacement vector \mathbf{X} respectively (for force \mathbf{F} , $F^{(1)}$ and $F^{(2)}$ will be used hereafter to denote the horizontal and vertical components respectively). Eq. (11) can be regarded as a ‘mixed-type’ boundary condition which blends the vertically forced oscillation, the clamped (build-in supported) condition and the horizontally unconstrained condition.

Eqs. (10) and (11) are the boundary conditions used in the FSI simulation of self-propelled flapping foils. In one validation case of this section, a simply supported (pinned) condition is also used, i.e.,

$$\begin{aligned} (\mathbf{X})_{s=0} &= \mathbf{X}_0, \\ \left(\frac{\partial^2 \mathbf{X}}{\partial s^2} \right)_{s=0} &= (0, 0). \end{aligned} \quad (12)$$

The details of the discretization procedure (including the discretization near the boundaries) are summarized in Appendix B.

To validate the structure solver, we first simulate a flexible filament moving under gravity in vacuum. The simply supported (pinned) boundary condition (Eq. (12)) is used at one end and the free-end boundary condition (Eq. (10)) is used at the other. The initial position of the filament is given by

$$\begin{aligned} \mathbf{X}(s, 0) &= \mathbf{X}_0 + (s \cos k, s \sin k), \\ \partial \mathbf{X}(s, 0) / \partial t &= (0, 0), \end{aligned} \quad (13)$$

where k is a constant and $\mathbf{X}_0 = (0, 0)$. At $t = 0$, the filament is released and starts swinging due to the gravitational force. We use

$\beta = 1.0, L = 1.0, Fr = 10.0, \mathbf{g}/g = (1, 0), \gamma = 0$ and $k = 0.01\pi$ as the control parameters. For the case where the swing amplitude is small and the bending force is neglected, an analytical solution in series form can be derived by using the perturbation method [39]. The numerically predicted free-end vertical position $Y(L, t)$ is compared with the analytical result in Fig. 2. From this figure, a good agreement between the two is clearly seen.

To further test the validity of the boundary condition Eq. (11) in a self-propelled system, we then simulate the forced oscillation of a flexible foil in vacuum. At the leading-edge, the boundary condition of Eq. (11) is imposed together with a vertically sinusoidal motion prescribed as $y(t) = 0.001 \cos(\omega_n t)$, where ω_n with $n = 1, 2, 3$ denotes the first three natural angular frequencies in a cantilever beam. At the trailing-edge, the free end boundary condition Eq.

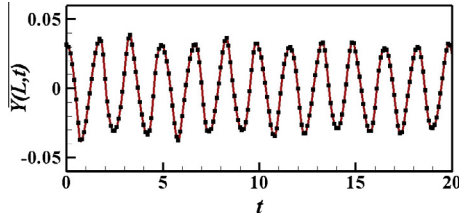


Fig. 2. The vertical free-end position of a hanging filament without ambient fluid under a gravitational force. The solid line denotes the result of the current study while the square denotes the analytical solution in Huang et al. [39].

(10) is used. For the cases of small forcing amplitudes, the solution of Eq. (3) is very close to that of an Euler–Bernoulli beam. The mode shapes of the foil are plotted in Fig. 3. It is seen that the first, second and third mode shape spontaneously emerges due to the application of forcing with the corresponding frequency. Unlike a conventional Euler–Bernoulli beam, however, in this case the horizontal displacements (including that of the leading-edge) are still permitted. Due to the inextensible constraint, the trajectories of both ends are of figure-eight type (see Fig. 4(a) and (b)). It is also seen from the figure that the vertical displacement of the leading-edge is much smaller than that of the trailing-edge. The time history of the streamwise displacement of the centroid is plotted in Fig. 4(c). Since the resultant horizontal force is zero, the streamwise displacement of the centroid should be identically zero. Our numerical result for the displacement of the centroid matches the exact solution to machine precision.

For reference purpose, the simulation of a rigid self-propelled flapping foil ($\gamma = \infty$) is also performed in this work. For this type of simulation, Eq. (3) can still be used by setting the bending rigidity γ to a very large value. However, a large bending force could result in severe numerical problems in the structure solver. Instead, we use the Newton's second law as the governing equation for the motion of a rigid foil in the horizontal direction:

$$\beta \frac{d^2 X_c}{dt^2} = - \sum_{j=1}^N F^{(1)}(\mathbf{X}_j, t) \Delta s, \quad (14)$$

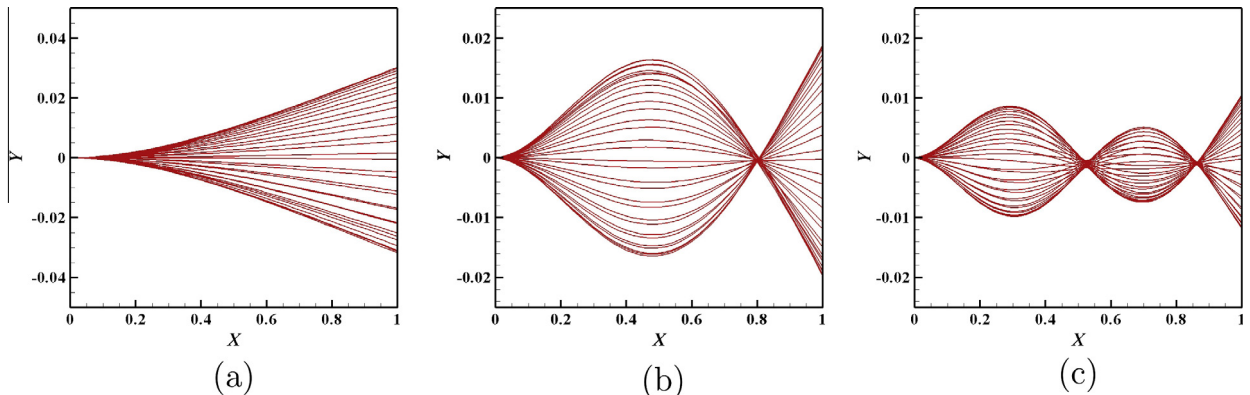


Fig. 3. The shapes of a self-propelled filament in the forced oscillation with a vertical motion of the leading-edge prescribed as $y = 0.001 \cos(\omega_n t)$, where $\omega_n = (k_n/L)^2 \sqrt{B/\rho_s}$ is the n th natural angular frequency of the Euler–Bernoulli cantilever beam. (a) $n = 1, \omega_1 = 3.52$; (b) $n = 2, \omega_2 = 22.0$; (c) $n = 3, \omega_3 = 61.7$. Positions of the foil are in the frame moving with the leading-edge and plotted every $\Delta t = T/30$, for one forcing period from $t = 6T$ to $t = 7T$, where T is the period of the forced oscillation. In computing the natural frequencies, we set $L = 1, B = 1, \rho_s = 1$. In the simulations, we use the dimensional form of Eq. (3) and also set $L = 1, B = 1, \rho_s = 1$.

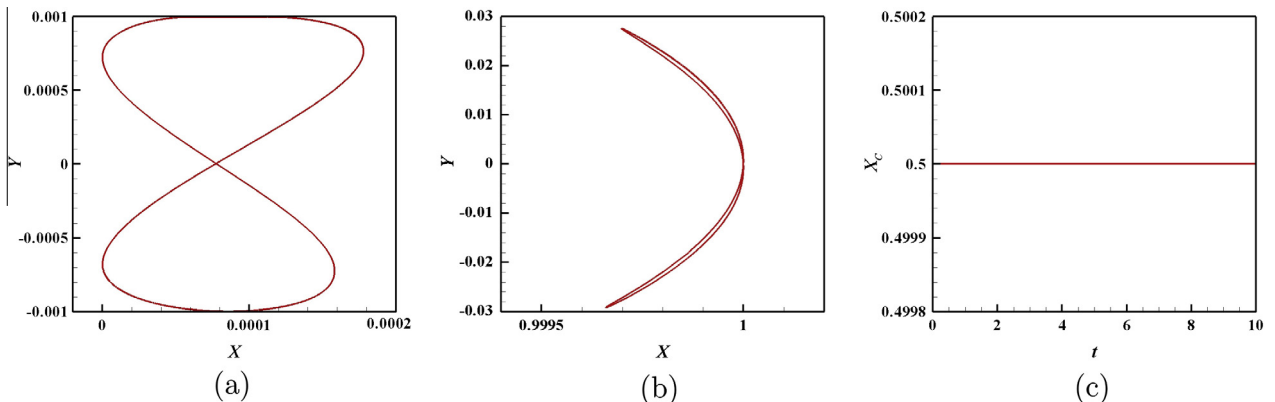


Fig. 4. The trajectories of the leading- and trailing-edge and the time history of centroid streamwise displacement of a self-propelled filament in vacuum under the forced oscillation of the first mode: (a) leading-edge trajectory; (b) trailing-edge trajectory; and (c) time history of the streamwise displacement of the centroid. All positions in the trajectories are in the laboratory frame and plotted every $\Delta t = T/30$, for one forcing period from $t = 6T$ to $t = 7T$, where T is the period of the forced oscillation.

where X_c is the horizontal position of the center of mass. An explicit scheme very similar to that for solving Eq. (3) is used for the temporal advancement of Eq. (14).

3.3. Fluid–structure coupling

We use a staggered or loosely-coupled method for the FSI problem, in which the flow solver and structure solver are alternatively advanced by one step in time. In the framework of the direct-forcing immersed boundary method, the velocity of the filament obtained in the structural solver provides one boundary condition for the fluid solver, i.e., $\mathbf{U}_b = \dot{\mathbf{X}}$; while the Lagrangian force \mathbf{F} determined in the flow solver acts as the source term in the structural equation (Eq. (3)).

To validate the coupled solver, we simulate the interaction of a flexible filament with a free stream at $Re = 200$. Other parameters used here are $\beta = 1.5$, $Fr = 0.5$, $\mathbf{g}/g = (1, 0)$ and $L = 1.0$. We use a computational domain of $16L \times 10L$. The distance between the leading-edge of the filament and the inlet is $6L$. The number of the Lagrangian points representing the filament is 50 and the mesh size in the vicinity of the filament (a region of $6L \times 2L$) is uniformly $0.02L$.

A uniform velocity is prescribed at the inlet; non-slip boundary conditions are imposed on the two lateral walls; a boundary condition which is equivalent to the constant-pressure condition is prescribed at the outlet. The boundary condition for the filament is the same as that of the first case (filament moving under gravity in vacuum) in Section 3.2. The initial condition for the entire fluid filed is a uniform flow (moving at the inlet velocity). To trigger the instability, the filament is initially placed inclined at an angle of 0.1π with respect to the flow direction.

Fig. 5 shows the time histories of the vertical positions of the trailing-edge for two different bending rigidities. It is seen that the present results agree well with those from Huang et al. [39] for both cases.

3.4. Simulation set-up and mesh-independent test

For the study of a self-propelled foil driven by vertical oscillation at the leading-edge, simulations were performed on a rectangular box of sizes $[-29L, 29L]$ $[-6L, 6L]$, in the streamwise and transverse direction respectively. The leading-edge of the foil is located at $(0, 0)$ initially (see Fig. 6). A locally-refined quadrilateral mesh with hanging-nodes is generated for the simulation. Within each sub-domain (I, II or III) shown in Fig. 6, the computational cells are uniform. The mesh sizes are $0.02L$, $0.04L$ and $0.08L$, in I, II and III, respectively and the resulting total cell number is 688,000. The number of the Lagrangian points representing the filament is 50.

Non-slip boundary conditions are imposed on the four sides of the computational domain for the fluid. The initial condition for the entire flow filed is zero-velocity condition. The foil initially aligns itself in the horizontal direction and is placed at the position of maximum vertical displacement, i.e., $\mathbf{X}(s, 0) = (s, \bar{A})$. The time

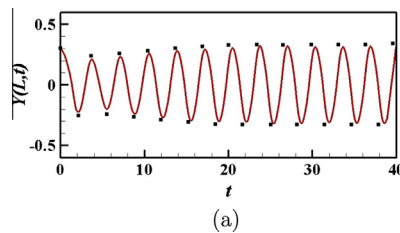


Fig. 5. Time history of the vertical position of the trailing-edge in the FSI of a flexible filament with a free stream at $Re = 200$: (a) $\beta = 1.5$, $\gamma = 0.0015$, $Fr = 0.5$ and (b) $\beta = 1.5$, $\gamma = 0.0$, $Fr = 0.5$. The solid line denotes the result of the current study while the square denotes the result in Huang et al. [39].

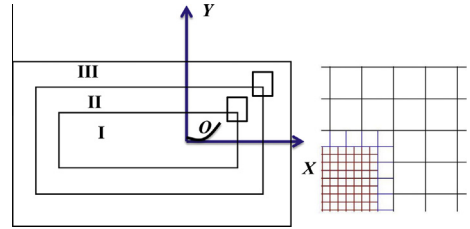


Fig. 6. Computational domain and locally-refined mesh with hanging-nodes for the study of a flexible self-propelled plunging foil. Three sub-domains with different mesh resolutions are shown. The enlarged view of a region where meshes with hanging-nodes are deployed is also shown.

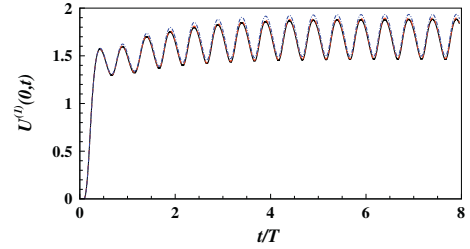


Fig. 7. Results of the mesh-independent test: leading-edge horizontal velocity as a function of time obtained by using three different meshes. $T = 2\pi/\bar{A}$ is the dimensionless period of the plunging motion. The dash-dotted line, dashed line and solid line denote the result for the grid size of $0.04L$, $0.02L$ and $0.01L$, respectively.

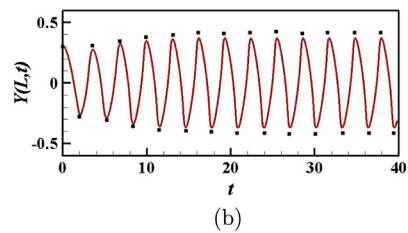
steps for the simulations are chosen such that the maximum *CFL* number (defined by the fluid velocity, time step and grid width) is 0.5.

Grid convergence tests have been conducted to ensure that the results obtained are independent of the mesh resolution. Fig. 7 shows the horizontal velocity of the leading-edge as a function of time for three different grid widths, $0.01L$, $0.02L$ and $0.04L$ (this is the mesh resolution in domain I, the grid widths are doubled and quadrupled in II and III, respectively). Other control parameters in this test are: $Re_f = 200$; $\bar{A} = 1.0$; $\beta = 0.2$; $\gamma = 4.0$. It is seen that comparing with the result for the grid width of $0.02L$, some deviation can be found if the grid width is double. However, (almost) identical result is obtained if the grid width is reduced to $0.01L$.

From Fig. 7, it is also seen that during the first half flapping period after starting, the forward speed undergoes a rapid increase from zero. Then a gradual increase in speed will last for about 3.5 flapping periods. A periodically steady state is achieved after four flapping periods.

4. Results and discussion

To investigate the role of flexibility on the hydrodynamics of a self-propelled flapping foil, we perform series of simulations by



varying the dimensionless bending rigidity while keeping other parameters fixed. In four cases A, B, C and D, four different combinations of mass ratio and oscillation amplitude are considered. The parameters used in the simulations are summarized in Table 1. Cases A and B are of $\beta = 0.2$, with the dimensionless driving amplitudes being 0.2 and 0.5 for case A and case B, respectively. Cases C and D are of $\beta = 2.0$, with the dimensionless driving amplitudes also being 0.2 and 0.5 for case C and case D, respectively. A relatively wide range of bending rigidity is chosen and 20–27 different bending rigidities are studied in each case. Moreover, for the highest bending rigidity studied, the important physical quantities (such as cruising speed and swimming power) obtained are indistinguishable with the reference values obtained on a rigid foil (see Section 3.2). In addition to the cases listed in Table 1, simulations are also performed at $\beta = 1.0, 4.0, 6.0, 8.0, 10.0$ for $\bar{A} = 0.2$ to determine the borders among different flow regimes (see Section 4.3 for the details). For each of the five different mass ratios above, six bending rigidities are considered.

4.1. Effects of flexibility on propulsive performance

First, the key physical parameters for quantifying the propulsive performance are defined as follows.

The cruising speed U_c is defined as the average horizontal velocity reached by the leading-edge of the foil at a (periodically) steady state, i.e.,

$$U_c = -\frac{1}{T_f} \int_0^{T_f} \left(\frac{\partial X}{\partial t} \Big|_{s=0} \right) dt, \quad (15)$$

where $T_f = 2\pi\bar{A}$ is the dimensionless flapping period. It should be noted that the cruising speed is not well-defined if the flow enters the non-periodic regime (to be discussed later).

The swimming power, which is the average input power required to produce the oscillation of the foil, can be defined as

$$P_s = \frac{1}{T_f} \int_0^{T_f} \left(\int_0^1 \left(\mathbf{F} \cdot \frac{\partial \mathbf{X}}{\partial t} \right) ds \right) dt. \quad (16)$$

Similarly, P_s is not well-defined if the periodic state is not reachable.

To quantify the propulsive efficiency of the self-propelled locomotion, in some recent works, an ‘efficiency factor’ defined as the ratio of thrust power to (input) swimming power has been used. However, the definition of efficiency factor is still controversial due to the ambiguities in calculating the ‘thrust power’ when the (average) resultant force in the horizontal direction equals zero. In Thiria and Godoy-Diana [33] and Ramananarivo et al. [34], the ‘thrust force’ was measured by holding the flapping foil in a fixed position. The force thus obtained was then used to calculate the thrust power. In Borazjani and Sotiropoulos [41], an arbitrary decomposition was used to separate the thrust and drag forces. In the current work, we follow the idea proposed by Kern and Koumoutsakos [42] and use a *propulsive parameter* defined as the ratio of the kinetic energy in the forward motion of the foil and the work done to the fluid by the foil over one forcing period. The amount of the work is computed as the time integral of the

swimming power [30]. In the mathematical formulation, the propulsive parameter is defined as

$$\eta = \frac{\frac{1}{2} \beta U_c^2}{T_f P_s}. \quad (17)$$

For reference purpose, the cruising speed, swimming power and propulsive parameter achieved in rigid foils are first computed and the results for the four cases are summarized in Table 2. When comparing the two cases with the same mass ratio (such as A and B or C and D), it is seen that higher forcing amplitude results in lower cruising velocity. This is very counter-intuitive at the first glance, however, it can be easily understood if one notice that higher amplitude is always accompanied by lower frequency, since the flapping Reynolds number is the same for all cases.

The evolution of normalized cruising speed, swimming power and propulsive parameter with increasing bending rigidity is shown in Fig. 8. The parameters listed in Table 2 are used as the reference quantities for the normalization. The overall trend shown in Fig. 8 is that the global maxima are not achieved in a rigid foil but a foil with some passive flexibility. A similar trend in cruising speed was also reported in [36]. In Fig. 8, besides the global maxima, local maxima are also found in some quantities, such as the cruising speeds for case A and case B. The bending rigidities for achieving the global maxima in normalized cruising speed, swimming power and propulsive parameter are summarized in Table 3. It is seen that for all cases studied, the locations of global maxima in cruising speed and propulsive parameter are very close to each other. The performance enhancement due to the adding of flexibility (in terms of propulsive parameter increase) is found to be more significant in the two cases of lower mass ratio (A and B). For the two cases of higher mass ratio (C and D), although the increase in cruising speed due to flexibility is also noticeable, lesser performance gain is mainly caused by the drastic increase in swimming power.

It is interesting to note that a similar trend has also been reported in some studies of the flexibility effect on hovering performance of flapping foils or wings [19,52]. In these works, the maximum *lift* production was achieved at a moderate flexibility. Moreover, the hovering performance (*lift-to-power ratio*) was found to deteriorate in foils/wings with higher mass ratios.

4.2. Resonance and performance optimum

In this section, we will explore the role of resonance (between the forcing and the natural frequency) in optimizing performance.

First, we define the reduced forcing frequency as $\bar{\omega} = \omega_f/\omega_1$, where ω_1 is the first natural angular frequency of the system. For cases of large mass ratios (where the influence of outside fluid can be neglected), the natural frequencies of the system are approximated by those of a clamped-free elastic sheet in vacuum. Thus for the cases of $\beta = 2.0$ (C and D), ω_1 is calculated analytically as

$$\omega_1 = \left(\frac{k_1}{L} \right)^2 \sqrt{\frac{B}{\rho_s}}, \text{ with } k_1 = 1.875. \quad (18)$$

Table 1

The control parameters in the simulations of the current study.

	Re_f	\bar{A}	β	γ
A	200	0.2	0.2	$10^{-3}-10^4$
B	200	0.5	0.2	$10^{-3}-10^4$
C	200	0.2	2.0	$10^{-1}-10^4$
D	200	0.5	2.0	$10^{-1}-10^4$

Table 2

The cruising speed, swimming power and propulsive parameter achieved in the rigid foils.

	U_c^∞	P_s^∞	η^∞
A	1.16	1.70	0.063
B	0.83	1.06	0.021
C	1.17	1.65	0.660
D	0.82	1.02	0.212

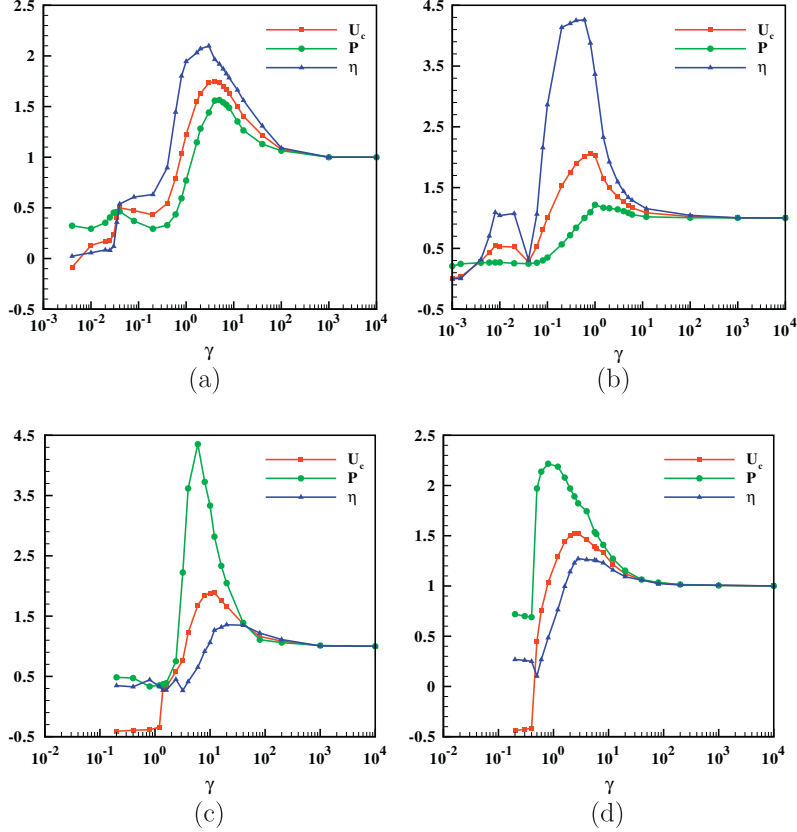


Fig. 8. Normalized cruising speed, swimming power and propulsive parameter as a function of γ : (a) case A; (b) case B; (c) case C; and (d) case D. The solid lines with squares denote the cruising speed; the solid lines with circles denote the swimming power; the solid lines with triangles denote the propulsive parameter. All quantities have been normalized by the values obtained in a rigid foil.

Table 3

The global maxima in normalized cruising speed, swimming power and propulsive parameter and the dimensionless bending rigidities corresponding to these maxima.

	$\gamma^{U_{\max}}$	$\frac{U_{\max}}{U_c^{\infty}}$	$\gamma^{P_{\max}}$	$\frac{P_{\max}}{P_s^{\infty}}$	$\gamma^{\eta_{\max}}$	$\frac{\eta_{\max}}{\eta^{\infty}}$
A	3.8	1.75	5.0	1.56	3.0	2.08
B	0.8	2.06	1.0	1.22	0.7	4.26
C	12.0	1.89	6.0	4.35	20.0	1.36
D	2.4	1.52	0.8	2.22	2.8	1.28

The reduced frequency then becomes

$$\bar{\omega} = \frac{\omega_f}{\omega_1} = \frac{2\pi f}{\omega_1} = \frac{1}{A} \frac{1}{k_1^2} \sqrt{\gamma}. \quad (19)$$

However, for the cases of small mass ratios, the natural frequencies of the system can be significantly modified due to the presence of outside flow [10]. In this work, we use the first natural frequency of a passive elastic sheet in axial flow as a better approximation to that of the current system. For cases of $\beta = 0.2$ (A and B), the linear stability analysis and an inviscid ‘vortex sheet’ representation of the wake are used to compute the first natural frequency (see the Appendix of [10]).

The evolution of the normalized cruising speed, swimming power and propulsive parameter with increasing reduced forcing frequency are shown in Fig. 9. It is seen that for all cases, the optimized cruising speed is obtained around $\bar{\omega} = 0.55$ – 0.65 , which is quite close to the experimental result (on flappers with high mass ratios) in Ramananarivo et al. [34]. For case A and B, the positions of the maxima in the swimming power and cruising

speed are almost coincident. For case C and D, the positions of maximum swimming power are shifted towards higher frequencies (around $\bar{\omega} = 0.8$ – 0.9). Note that the trend of swimming power obtained in this work seems to be quite different from that in [34], where the power was found to increase monotonically with increasing reduced forcing frequency. We remark that this seeming contradiction is caused by the different reference values used in the non-dimensionalization procedure. More specifically, $\rho_f U_{ref}^3 L^2$ is used in our work to non-dimensionalize the power, while BU_{ref}/L (or $\gamma \rho_f U_{ref}^3 L^2$) was used in theirs. As to the propulsive parameter, it is seen that the maximum is achieved at $\bar{\omega} = 0.7$ and $\bar{\omega} = 0.75$, for case A and B, respectively. For case C and D, the maxima for the propulsive parameter are achieved around $\bar{\omega} = 0.5$. All the results indicate that for optimizing cruising speed and propulsive efficiency, the flapping foil may stay much below the resonance point. This observation is consistent with the finding in [34]. We also noted that in a recent study [52] on the role of flexibility in the hovering performance of a rectangular flapping wing, the maximum lift and efficiency (lift-to-power ratio) were also achieved at a forcing frequency much lower than the resonance point (around $\bar{\omega} = 0.25$ – 0.35).

Due to the lack of a large bank of comparative resonant frequencies and wing/tail beats of animals, it is still not possible to establish a firm connect between our observation and flapping-based animal locomotion. However, evidences have been found that some insects are indeed operating at the reduced frequency around $\bar{\omega} = 0.5$. Two such examples are the hoverfly and the dragonfly. Based on the measured chordwise flexural stiffness, the natural frequencies of the wing are 324 Hz and 90 Hz, respectively for hoverfly [43] and dragonfly [44]; while theirs wing-beat frequencies are 160–180 Hz and 35–45 Hz, respectively.

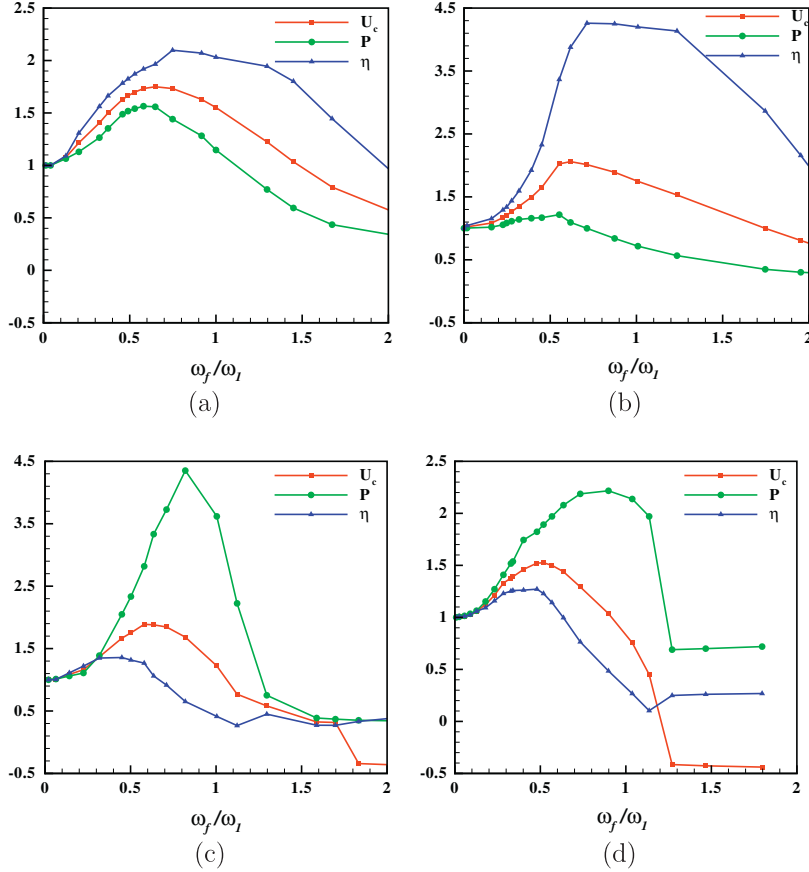


Fig. 9. The normalized cruising speed, swimming power and propulsive parameter as a function of reduced forcing frequency: (a) case A; (b) case B; (c) case C; and (d) case D. The solid lines with squares denote the cruising speed; the solid lines with circles denote the swimming power; the solid lines with triangles denote the propulsive parameter. All quantities have been normalized by the values obtained in a rigid foil.

4.3. Influence of flexibility on flapping amplitude and mode shape

First we examine the absolute and relative trailing-edge amplitudes, which are two important quantities for describing the shape of a flexible foil. The absolute trailing-edge amplitude A_T is defined as the amplitude in the laboratory frame, while the relative trailing-edge amplitude A'_T is defined as that in the frame moving with the leading-edge. Note that both amplitudes defined here are dimensionless quantities (which are normalized by the filament length L).

The evolution of absolute and relative trailing-edge amplitudes with increasing bending rigidity for the four cases is shown in Fig. 10. In the plots of absolute amplitudes, two maxima are found in case A, while three are found in case B. The two peaks in A from right to left correspond to the resonance at the first and second natural frequencies, respectively. The three peaks in B from right to left correspond to the resonance at one third of the first natural frequency, the first and second natural frequencies, respectively. For the relative amplitudes of case A and case B, some peaks of are distorted (flattened). This phenomenon has also been observed before in [10]. For case C and case D, one global peak is clearly seen in both the absolute and the relative amplitudes (see Fig. 10(c) and (d)). The peaks of the relative amplitudes are almost coincident with those of the absolute amplitudes, although a small shift towards the left can be seen. These peaks correspond to the resonance at the first natural frequency. For cases D, another tiny peak in the absolute amplitude is also seen. This tiny peak corresponds to the resonance at one third of the first natural frequency.

To further elucidate the relationship between peak absolute amplitudes and the occurrence of resonance, the absolute ampli-

tude (normalized by the value obtained in rigid foil) is also plotted as a function of reduced forcing frequency in Fig. 11. For cases C and D, the global maxima are always achieved at $\bar{\omega} = 1.0$, indicating regular resonant behavior. For cases A and B, however, the distortion of the resonance curve is quite obvious. First, the values of resonance peaks are smoothed. Second, the resonance peaks are shifted towards higher frequencies. Comparing with that in case A, the distortion of the resonance curve in case B (which has a larger flapping amplitude) is more noticeable. The distortion of resonance curve can be attributed to the nonlinear damping effect of the fluid drag [34]. In cases of small mass ratios, the fluid drag is relatively important if compared with the inertial force of the foil, thus significant distortion is observed in the resonance curves. Furthermore, the distortion intensifies with the increase of flapping amplitude. In cases of large mass ratios (such as C and D), the fluid drag becomes less important. Thus the distortion of the resonance curve is not clearly seen. In Fig. 11, tiny peaks are also observed in the nearness of one third of the first natural frequency in cases B and D (although it is hard to identify in case D). The occurrence of superharmonic resonance at $\omega_1/3$ for large flapping amplitudes has also been reported in [34].

Next we will look at the mode shapes at various bending rigidities for case A and case D. The mode shapes for case B and case C are very similar to those for case A and D, respectively. Thus the mode shapes of these two cases are not shown here for brevity. The mode shapes for case A are shown in Fig. 12. The phase plots of the free-end (vertical velocity vs. vertical displacement) and the normalized power spectra of the free-end vertical displacement are also presented. The flapping of mode-1 type is clearly seen at $\gamma = 3.8$ (corresponding to the maximum cruising speed),

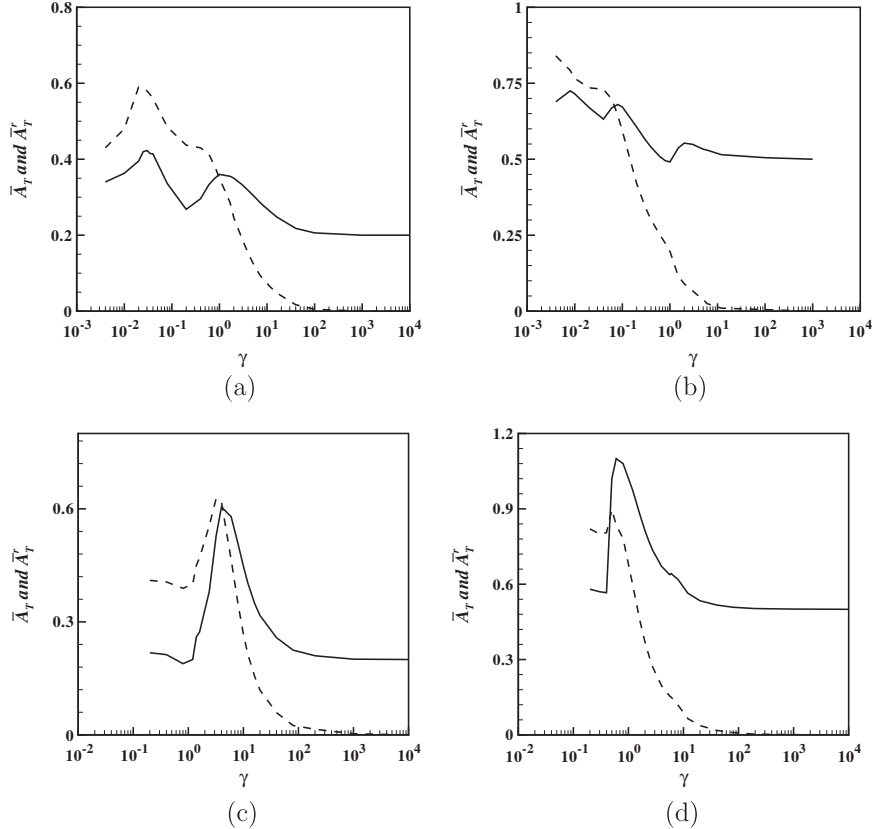


Fig. 10. Absolute and relative amplitude of the trailing-edge as a function of γ : (a) case A; (b) case B; (c) case C; and (d) case D. Solid line and dashed line denote the absolute and relative amplitude respectively.

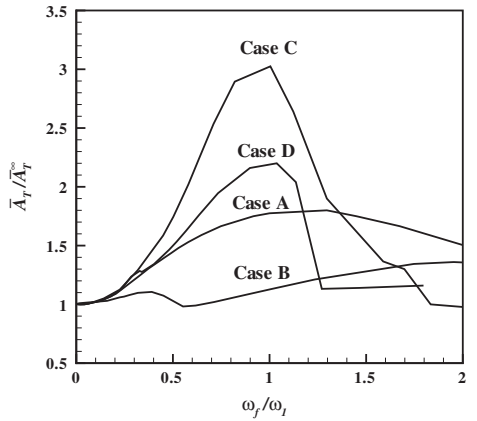


Fig. 11. Absolute amplitude of the trailing-edge as a function of reduced forcing frequency.

$\gamma = 1.0$ (corresponding to the rightmost peak of the absolute trailing-edge amplitude) and $\gamma = 0.2$ (corresponding to the trough between the two successive peaks of the absolute trailing-edge amplitude). It is also observed that the envelope of mode shape at $\gamma = 0.2$ is even wider than that at $\gamma = 1.0$. This seeming contradiction is caused by the change of frame, since the relative amplitude at $\gamma = 0.2$ is indeed higher than that at $\gamma = 1.0$. The phase plots at these three bending rigidities resemble that of a period-one limit-cycle (with frequency f) in appearance, although a small peak at $3f$ does exist in the power spectra. At $\gamma = 0.035$ (corresponding to the leftmost peak of the absolute trailing-edge amplitude), the flapping is of mode-2 type. It is interesting to see that the

up-down symmetry of the flapping is lost in this case. As that will be shown later, this asymmetric flapping is associated with the net lift caused by the symmetry breaking of the wake. At $\gamma = 0.025$, the flapping is also of mode-2 type but the up-down symmetry is almost recovered. At $\gamma = 0.004$ (corresponding to periodic backward-movement), the mode shape looks like the one formed by a beating cilium (but with a much larger Re number) and the up-down symmetry is fully recovered. The backward motion in a self-propelled flapping system has also been reported previously in Spagnolie et al. [29] and Zhang et al. [30], in the study of a self-propelled flexible foil based on the ‘lumped-torsional’ model. This backward-swimming mode is rather counter-intuitive and more discussions will be presented later in this subsection to better understand its origin. At these three bending rigidities ($\gamma = 0.035$, $\gamma = 0.025$ and $\gamma = 0.004$), the phase plots are characterized by the multiperiodic limit-cycle (with f , $3f$ and $5f$ as the dominating frequencies). At $\gamma = 0.001$, the flapping exhibits sustained non-periodic behavior, which can be characterized by the irregular trajectories in the phase plot and the multiple peak frequencies in the power spectrum.

The mode shapes for case D are shown in Fig. 13, together with the free-end phase plots (vertical velocity vs. vertical displacement) and the normalized power spectra of the free-end vertical displacement. It is seen that the flapping is of mode-1 type for all bending rigidities studied here. At $\gamma = 2.4$ (corresponding to the maximum cruising speed), the envelope of the mode shape is very narrow due to the low relative amplitude of the trailing-edge. At $\gamma = 0.8$ (corresponding to the maximum absolute amplitude), the envelope becomes much wider than that at $\gamma = 2.4$. After a careful examination of the envelope, it is found that the up-down symmetry of the flapping is *lost* at this bending rigidity. The excursion of

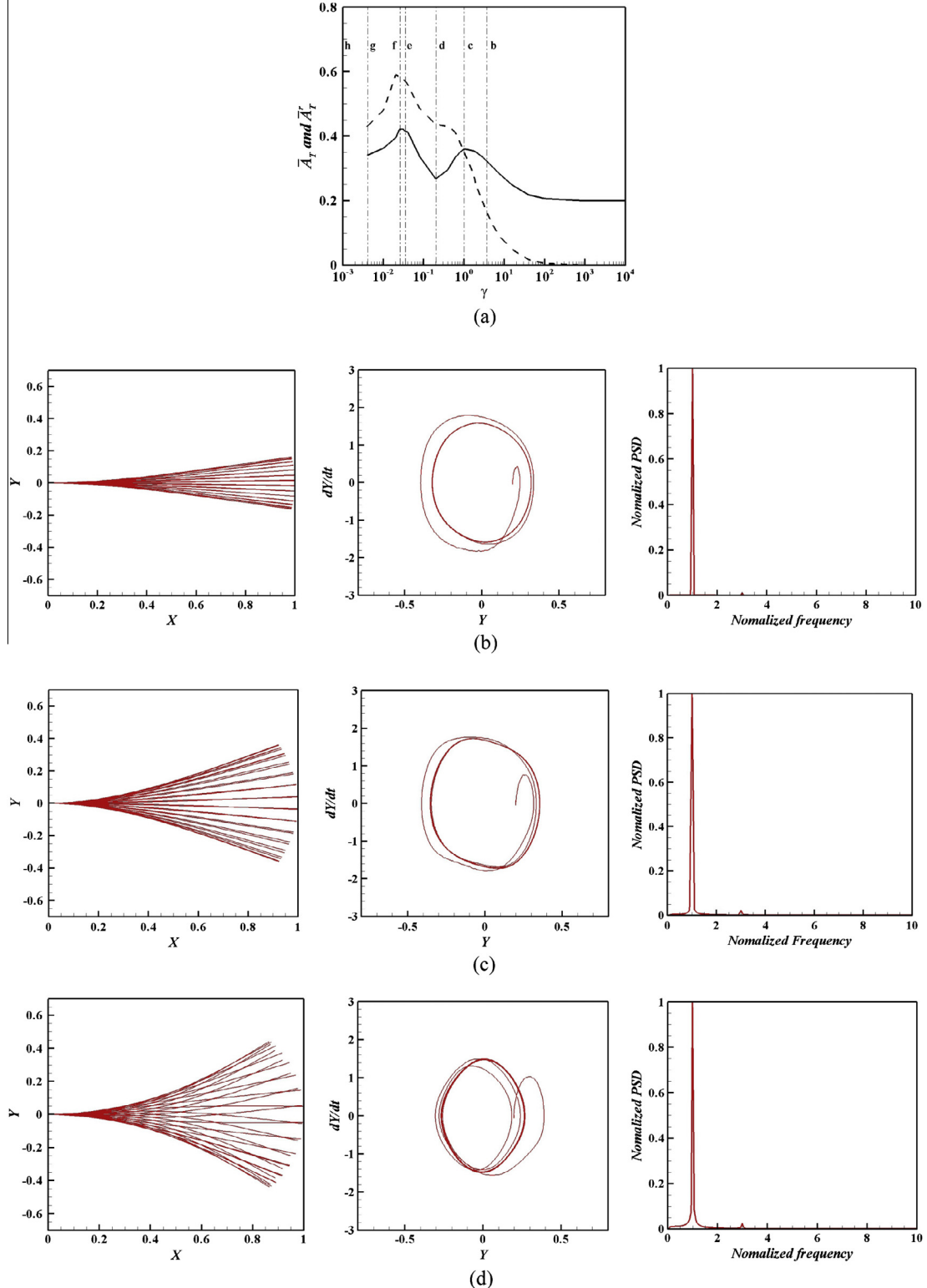


Fig. 12. Mode shape, phase plot of free-end (vertical velocity vs. vertical displacement) and normalized power spectrum of free-end vertical displacement, plotted for case A at various bending rigidities. Absolute and relative amplitude as a function of bending rigidity is also plotted in (a) for reference purpose; (b) $\gamma = 3.8$ (maximum cruising speed); (c) $\gamma = 1.0$ (rightmost peak in absolute amplitude); (d) $\gamma = 0.2$ (though between two successive peaks in absolute amplitude); (e) $\gamma = 0.035$ (leftmost peak in absolute amplitude); (f) $\gamma = 0.025$; (g) $\gamma = 0.004$ (backward-movement); and (h) $\gamma = 0.001$ (non-periodic flapping). The positions in the mode shape are plotted very 1/30 of the forcing period and are in the frame moving with the leading-edge. The displacement and velocity in the phase plot are in the laboratory frame. The frequency in the power spectrum has been normalized by f .

the trailing-edge is slightly tilted downwards. As it will be shown later, this asymmetric flapping is again associated with the symmetry breaking of the wake. The phase plots at these two bending

rigidities resemble that of a period-one limit-cycle (with frequency f) in appearance, however a small peak at $3f$ can still be found in the power spectra. At $\gamma = 0.4$ (corresponding to periodic

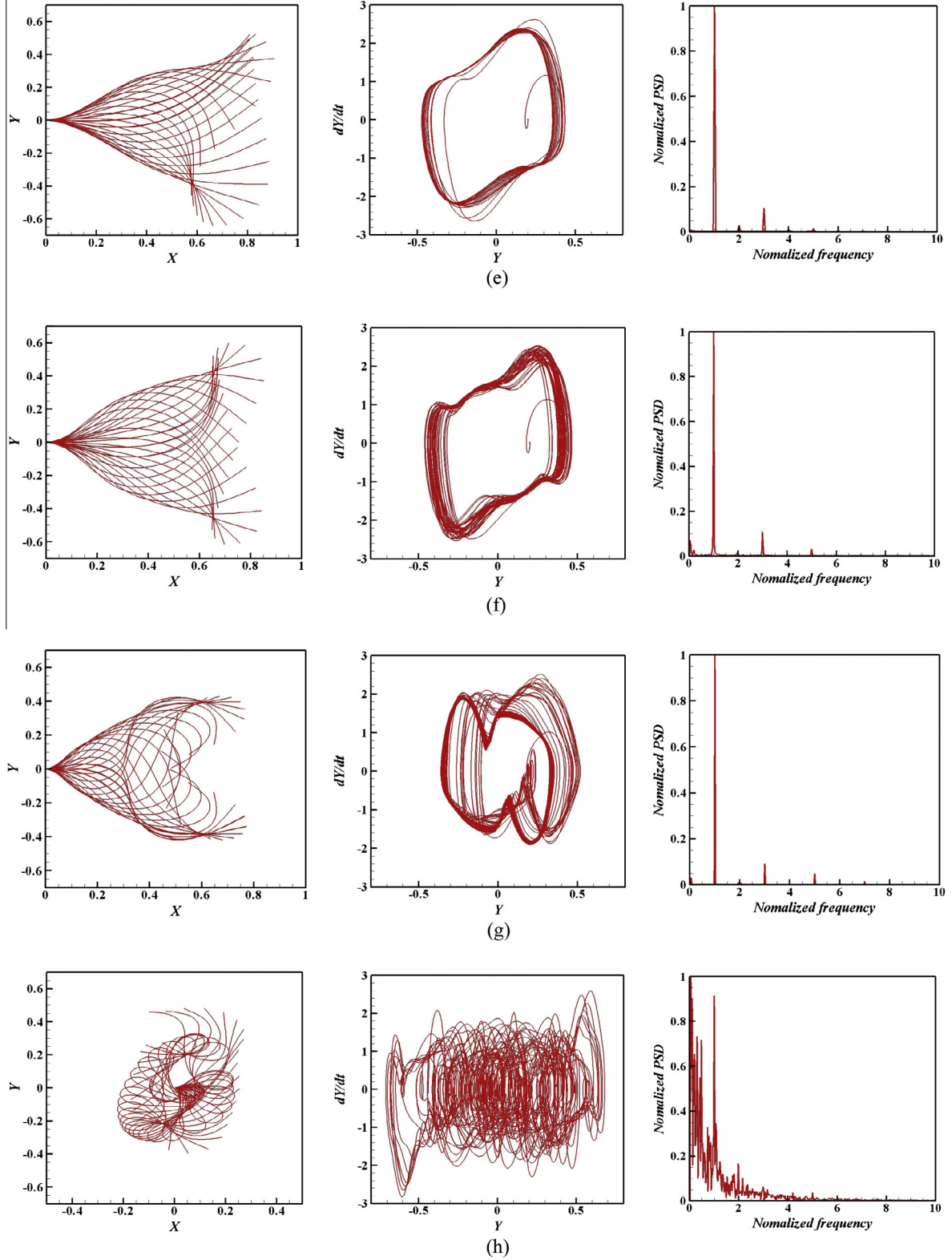


Fig. 12 (continued)

backward-movement), the up-down symmetry is recovered and the mode shape resembles that of a beating cilium (but with a much larger Re number). The phase plot is now characterized by the multiperiodic limit-cycle. In the power spectrum, six dominating frequencies ($1f$, $2f$, $3f$, $5f$, $6f$ and $7f$) arise. At $\gamma = 0.12$ (corresponding to non-periodic state), the flapping is characterized by

the irregular trajectories in the phase plot and the multiple peak frequencies in the power spectrum. In all the power spectra shown in Figs. 12 and 13, $3f$ always arises as one of the dominating frequencies (except those associated with non-periodic state). This is consistent with the fact that superharmonic resonance can occur at one third of the first natural frequency.

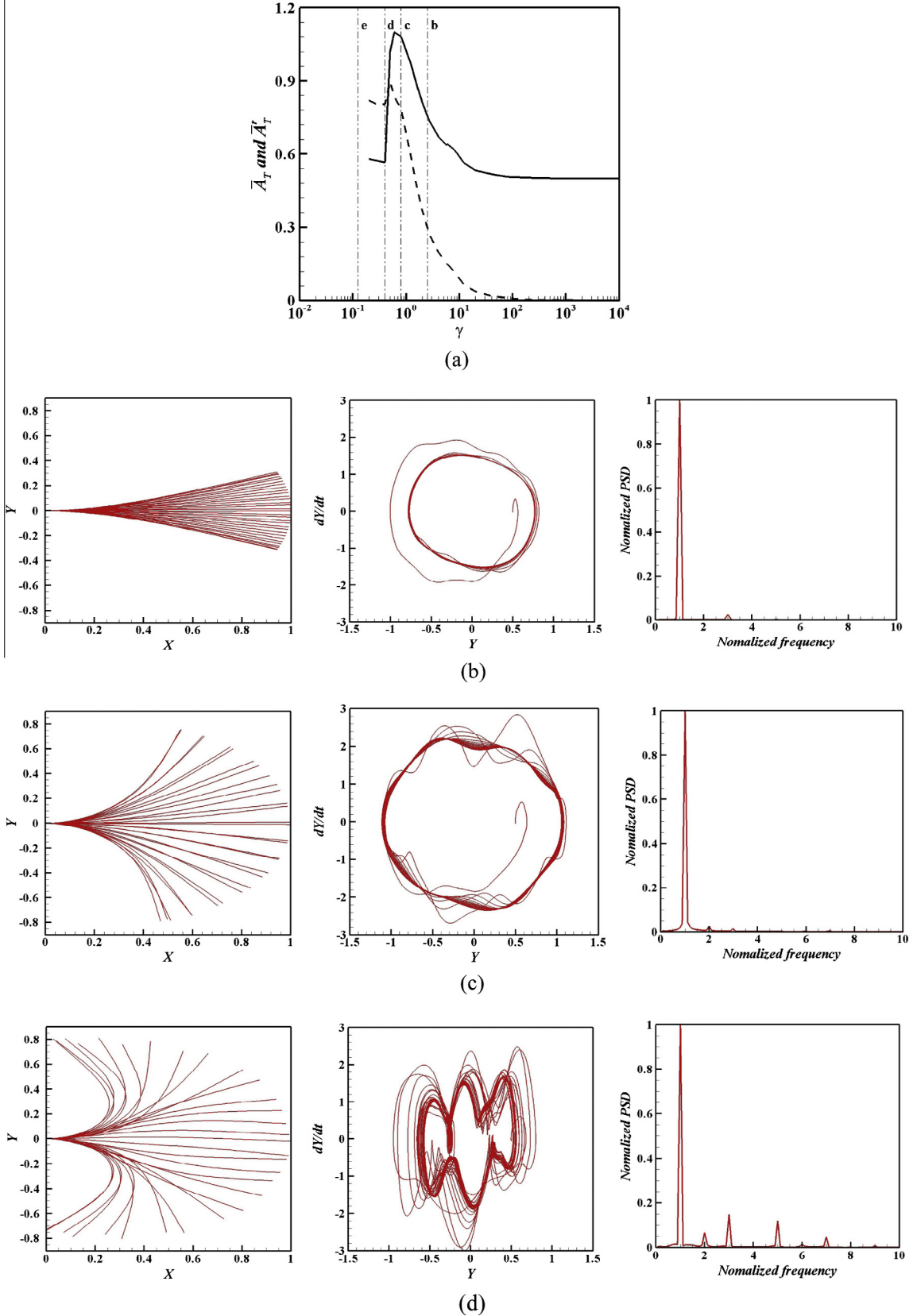


Fig. 13. Mode shape, phase plot of free-end (vertical velocity vs. vertical displacement), and normalized power spectrum of free-end vertical displacement, plotted for case D at various bending rigidities. Absolute and relative amplitude as a function of bending rigidity is also plotted in (a) for reference purpose; (b) $\gamma = 2.4$ (maximum cruising speed); (c) $\gamma = 0.8$ (maximum absolute amplitude); (d) $\gamma = 0.4$ (backward-movement); and (e) $\gamma = 0.12$ (non-periodic flapping). The positions in the mode shape are plotted very 1/30 of the forcing period and are in the frame moving with the leading-edge. The displacement and velocity in the phase plot are in the laboratory frame. The frequency in the power spectrum has been normalized by f .

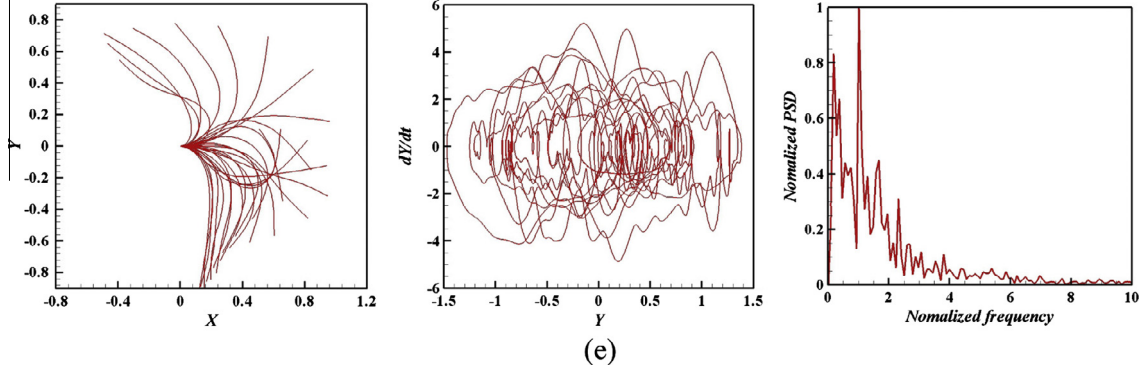


Fig. 13 (continued)

If we compare the result for case A (or case B) with that in [10] (where an inviscid model was used to study the thrust performance of a flexible heaving foil), the evolution of mode shape with increasing flexibility is very similar. A different trend of evolution for the mode shape was reported in the work by Dai et al. [53], where the thrust performance of a flexible low-aspect-ratio *pitching* plate was investigated. They found that the mode-2 deformation can appear not only when the rigidity is very low but also when the pitching amplitude becomes very high. If we compare the propulsive efficiency for different modes in the present study, it is seen that the mode-1 deformation has much higher efficiency than the other modes. Similar findings were also reported in [10,53].

Based on the flapping modes observed, the dynamical states of the self-propelled foil can be classified into three types: non-periodic, periodic backward and periodic forward. For cases A, C and D, with the increase of bending rigidity, the dynamical state may transit from non-periodic to periodic backward and then to periodic forward. However, for case B, with the increase of bending rigidity, the dynamical state transits directly from non-periodic to periodic forward. Such transition is also confirmed in the evolution of wake structure with bending rigidity (see the relevant discussions in Section 4.4). Further study indicates that the transition borders among the three dynamical states can be significantly affected by the mass ratio β . To investigate this issue, additional simulations (besides those in cases A and C) are performed at $\beta = 1.0, 4.0, 6.0, 8.0, 10.0$ for $\bar{A} = 0.2$ and different dynamical states are labeled in the $(\beta, 1/\bar{\omega})$ phase diagram (see Fig. 14(a)). The two borders separating the three regimes are determined

approximately using a series of simulations and illustrated as the two solid curves. It is seen that at the limit of $\beta \rightarrow \infty$, the transition from forward-movement to backward movement occurs at $\bar{\omega} = 1.62$; while the transition from backward-movement to non-periodic state occurs at $\bar{\omega} = 3.57$. Moreover, we also find that at the limit of $\beta \rightarrow \infty$, the maximum cruising speed is achieved at $\bar{\omega} = 0.55$. Again, it is confirmed that for the entire range of mass ratio (0.2–10.0) studied here, flappers cannot optimize their performance by operating near the resonance point. The missing of the periodic backward state in case B can be explained using the schematic display shown in Fig. 14b). From this figure, it is seen that for the mass ratio below a critical value β^* , the direct transition from non-periodic state to periodic forward state is possible. Such transition is not observed in case A, C and D since the mass ratios are above the critical value.

The phase difference α between the trailing- and the leading-edge is another important quantity for describing the shape of the flexible flapping foil. This quantity is found to be closely related to performance optimization. The phase difference at the maximal cruising velocities for the four cases are listed in Table 4. Here positive sign symbolizes a phase lead while negative sign symbolizes a phase lag in the trailing-edge. From Table 4, it is seen that the phase difference corresponding to the maximum velocity is close to $-\pi/4$, although some discrepancies do exist. For better understanding of the relationship between performance optimum and phase difference, the schematic representation of different shapes of the flexible foil (at the moment when the leading-edge passes the equilibrium position with a downward velocity) corresponding to various phase difference is shown in Fig. 15. For $\alpha = 0$, the trail-

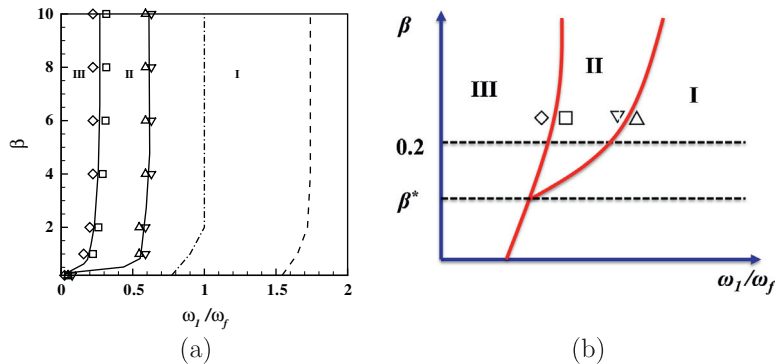


Fig. 14. Regimes of different dynamical states of the foil in the parametric space $(\beta, 1/\bar{\omega})$ for $\bar{A} = 0.2$. (a) the whole picture and (b) a close-up view near $\beta = 0$ (schematic diagram). I: periodic forward-movement; II: periodic backward-movement; and III: non-periodic state. Symbols ∇ and Δ correspond to some typical cases near the boundary between regime I and II, representing the periodic forward-movement and periodic backward-movement, respectively. Symbols \square and \diamond correspond to some typical cases near the boundary between regime II and III, representing the periodic backward-movement and non-periodic state, respectively. The dash-dotted line denotes the place where maximum absolute amplitude is reached; the dashed line denotes the place where maximum cruising speed is reached.

Table 4

The phase difference α between the trailing- and leading-edge and the ratio of angle of attack to trailing-edge deflection angle θ/ϕ (averaged over half plunging cycle) at the optimized cruising velocities for the four cases.

	α^{max,u_c}	$ -\pi/4 - \alpha^{max,u_c} /(\pi/4)$ (%)	$(\theta/\phi)^{max,u_c}$	$ (\theta/\phi)^{max,u_c} - 1.0 /1.0$ (%)
A	-0.76	3	0.91	9
B	-0.88	12	0.93	7
C	-0.87	11	1.03	3
D	-0.79	1	1.01	1

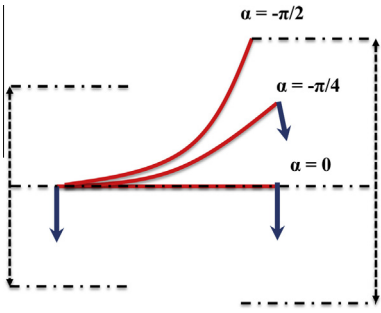


Fig. 15. A schematic representation of various shapes of the flexible foil for different phase angles at the moment when the leading-edge passes the equilibrium point with a downward velocity.

ing-edge moves in phase with the leading-edge, this scenario is only observed in a *rigid* foil. For $\alpha = -\frac{\pi}{2}$, the trailing-edge is about to reverse its direction when the leading-edge passes the equilibrium position thus very large relative amplitude can be achieved. This scenario is observed if the flexible foil operates near the resonance point. The shape for $\alpha = -\frac{\pi}{4}$ lies in between that for $\alpha = 0$ and that for $\alpha = -\frac{\pi}{2}$. The performance optimum achieved around $\alpha = -\frac{\pi}{4}$ can be explained by the ‘streamlined’ shape formed in the flexible foil. Here we examine two characteristic angles which are defined as follows (see Fig. 16). The first one is the effective angle of attack $\phi = \arctan(U_{flap}/U_c)$, where $U_{flap} = |\dot{y}|$ is the flapping velocity due to the plunging motion. The other one is the deflection angle θ of the trailing-edge. In [34], it was speculated that performance can be optimized if the trailing-edge aligns with the flow, i.e., $\theta = \phi$, when the leading-edge passes the equilibrium position ($U_{flap} = U_{ref}$). To further explore this issue, we compute the values of θ/ϕ when the leading-edge passes the equilibrium position for the scenarios in which the optimal cruising speeds are achieved and found that θ/ϕ is only around 0.5–0.6. We then compute the average values of θ/ϕ over half-cycle of plunging (either upstroke or downstroke). It is found that when the optimal cruising speed is reached, the averaged values of θ/ϕ are very close to unity in all cases studied (see Table 4). Based on this observation, we believe that in an average sense, $\theta \approx \phi$ is valid for performance optimum in a self-propelled flexible foil. The performance for $\alpha = 0$ (rigid foil) and $\alpha = -\frac{\pi}{2}$ (flexible foil operating near resonance point)

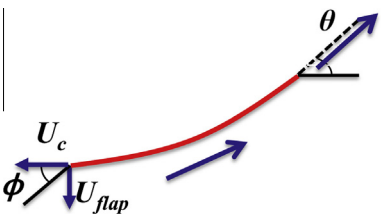


Fig. 16. The definitions of effective angle of attack and trailing-edge deflection angle.

are far from optimum due to the non-streamlined shapes formed. The relationship between streamlined shape and performance optimum can be further explained in the context of the forming of leading-edge and trailing-edge vortices. On one hand, the streamlined shape reduces the intensity of leading-edge vortices by reducing the scale of flow separation. On the other hand, for a foil with streamlined shape, sufficiently strong trailing-edge vortices are still produced. We believe that the two aspects above lead to the high propulsive performance of the system.

Another scenario which deserves more analysis is the shape for $\alpha < -\pi$, which corresponds to the backward-swimming mode. In Fig. 17(a) and (b), we compare the shapes of the flexible foil during upstroke in the backward swimming and forward swimming modes for case D. The two averaged shapes over half plunging cycle (upstroke) for the backward swimming and forward swimming modes are shown in Fig. 17(c). From the shape shown in Fig. 17(c), the seemingly counter-intuitive motion in the backward swimming mode can be easily understood by the fact that the flapper pushes fluid towards the left and thus propels itself towards the right.

4.4. Influence of flexibility on wake structure

To characterize the vortex shedding behaviors in flapping wings, the Strouhal number (St) has been widely used in the literature [45]. In this work, we define the amplitude-based Strouhal number as

$$St = \frac{2fA_T}{|\tilde{U}_c|} = \frac{1}{\pi} \frac{U_{ref}}{|\tilde{U}_c|} \frac{A_T}{A} = \frac{1}{\pi |U_c|} \frac{\bar{A}_T}{\bar{A}}, \quad (20)$$

where \tilde{U}_c is the dimensional cruising velocity; A and A_T are the dimensional amplitudes of the leading- and trailing-edge, respectively. Unlike that for a tethered foil placed in the uniform flow, the Strouhal number for a self-propelled foil is the result of the fluid-structure interaction problem and is *a priori unknown*.

For the Strouhal numbers observed in nature (including those in flying and swimming), 0.2–0.4 is considered to be the optimized range [46]. The results of this work indicate that the optimized range of Strouhal number can be achieved in a very wide range of bending rigidity (see the St – γ diagrams shown in Figs. 18(a), 19(a), 20(a) and 21(a)). It is observed that for all cases studied in this work, the Strouhal numbers in *rigid* foils always lie in the optimized range. It is also seen that the Strouhal numbers corresponding to the maximum cruising velocities are also in the range of 0.2–0.4, with case B being the only exception, where Strouhal number is slightly lower than 0.2 within a narrow range of bending rigidity centered around the value for achieving the maximal cruising speed (see Fig. 19(a)). The observations above suggest that the Strouhal number is not the only indicator for measuring efficiency. For a fixed Strouhal number in the optimized range, detailed vortex dynamic features (such as the intensities of the leading- and trailing-edge vortices) are still needed to determine the efficiency of the system.

We now look at the evolution of wake structure with the variation of bending rigidity. Fig. 18 shows the instantaneous vorticity contours for case A. At $\gamma = \infty$, $\gamma = 3.8$ and $\gamma = 0.4$, symmetric vortex streets are observed. The only difference (in the wake structure) among them is the spacing between two neighboring vortices in the vortex street. Obviously, different spacing is due to the different cruising velocities achieved. At $\gamma = 0.035$, a deflected vortex street is observed. Unlike the deflected vortical structures in the wake of a rigid flapping foil, this non-symmetric vortex-street is accompanied by the up-down non-symmetric flapping (see the mode shape in Fig. 12(e)). At $\gamma = 0.004$, which corresponds to the backward-swimming mode, the vortex street is not

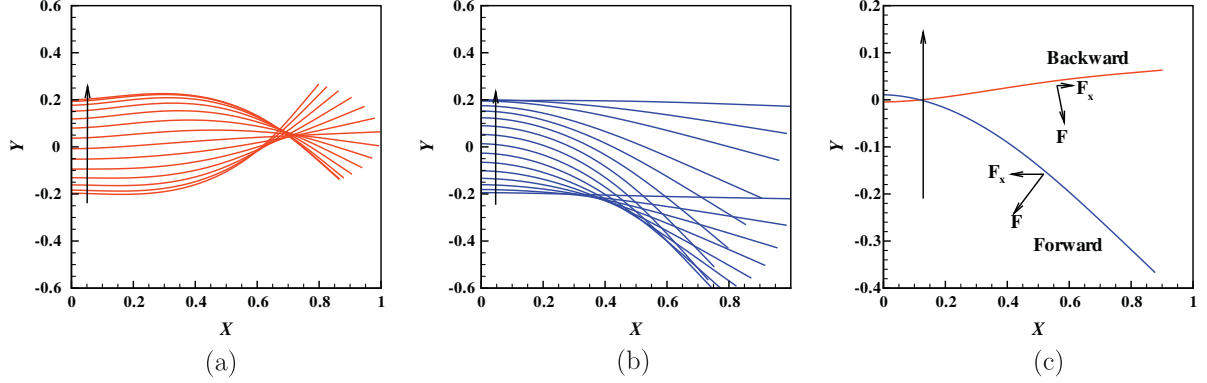


Fig. 17. The comparison of the shapes of the flexible foil during upstroke in backward swimming and forward swimming modes of case D: (a) 15 snapshots in backward swimming mode; (b) 15 snapshots in forward swimming mode; and (c) the averaged shapes over half plunging cycle (upstroke) in backward swimming and forward swimming modes. The averaged fluid forces (resultant forces and streamwise components) exerted on the foils are also plotted. The positions of the flexible foil plotted in this figure are in the frame which moves with the leading-edge horizontally but is static in the vertical direction. The snapshots in (a) and (b) are taken very 1/30 period. Red lines denote the shapes in the backward swimming mode; blue lines denote the shapes in the forward swimming mode. (For interpretation of the references to color in this figure legend, the reader is referred to the web version of this article.)

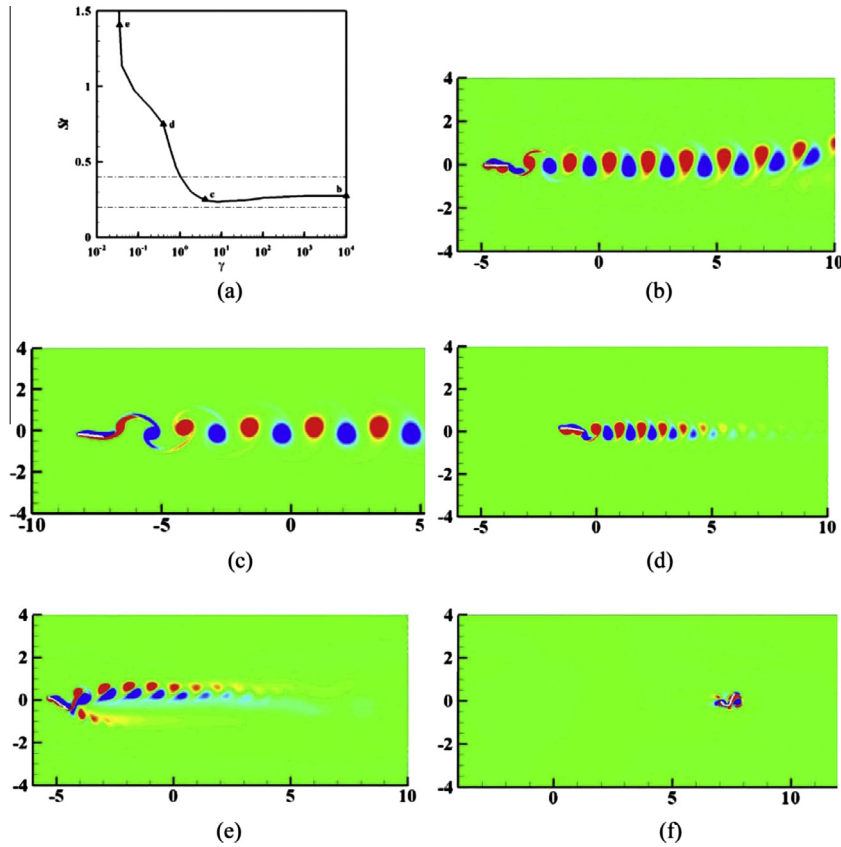


Fig. 18. Instantaneous vorticity contours for case A at various bending rigidities. St number as a function of bending rigidity is also plotted in (a) for reference purpose; (b) $\gamma = \infty$ ($St = 0.28$); (c) $\gamma = 3.8$ ($St = 0.25$); (d) $\gamma = 0.4$ ($St = 0.75$); (e) $\gamma = 0.035$ ($St = 1.4$); and (f) $\gamma = 0.004$ ($St = 5.41$). The contour color range is from -2.0 to 2.0 . The red color represents positive (counterclockwise) vorticity while the blue color represents negative (clockwise) vorticity. Case (f) is not labeled in (a) since the St number lies too far beyond the optimized range. (For interpretation of the references to color in this figure legend, the reader is referred to the web version of this article.)

observed due to the fact that the Reynolds number based on the cruising velocity is very small (around 20). Instead, structures of high vorticity concentration are only found in the very near wake. Note that the St number defined in Eq. (20) is not appropriate for characterizing the wakes of the backward-swimming mode, a more suitable quantity will be the Strouhal number based on the amplitude of the *leading-edge*.

For case B, the transition of the wake structure with decreasing γ is similar to that in case A. However, there are still some

difference between them, especially at higher bending rigidities (see Fig. 19). At $\gamma = \infty$, a deflected (non-symmetric) vortex street with large deflection angle is observed. At $\gamma = 0.8$ (where maximum cruising velocity is achieved), it is seen that the up-down symmetry of the vortex street is preserved. If we compare this wake with the symmetric vortex street in case A (see Fig. 18(c)), the difference can be clearly seen. At $\gamma = 0.8$ in case B, two vortices with the same sign are shed downstream in one half-cycle (it is termed as 2P-mode in some references while the vortex structure

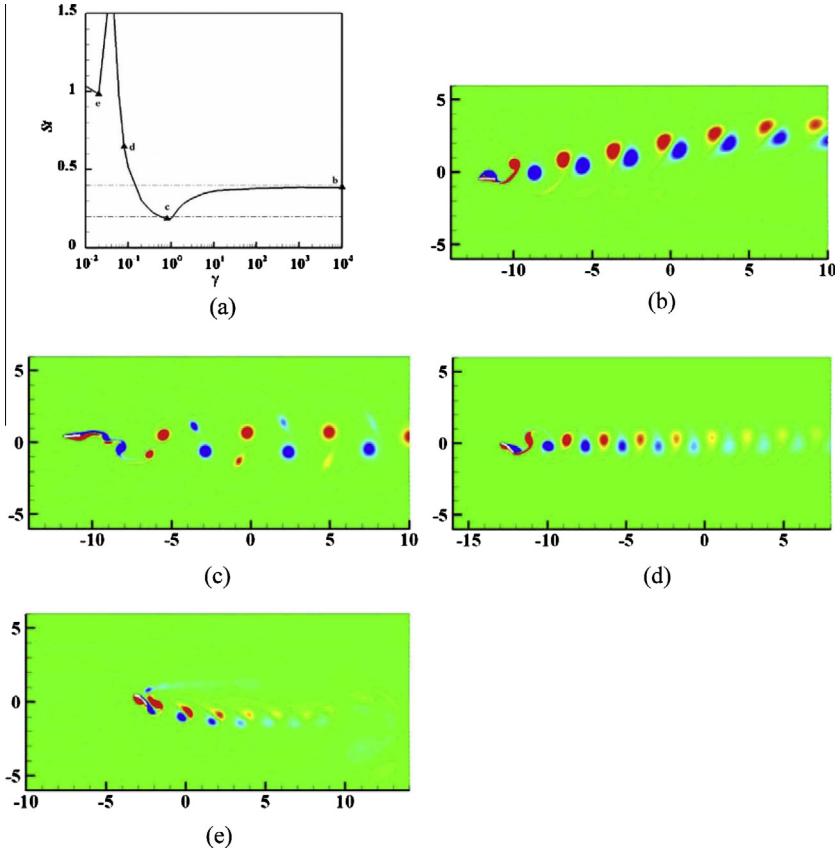


Fig. 19. Instantaneous vorticity contours for case B at various bending rigidities. St number as a function of bending rigidity is also plotted in (a) for reference purpose; (b) $\gamma = \infty$ (St = 0.38); (c) $\gamma = 0.8$ (St = 0.18); (d) $\gamma = 0.08$ (St = 0.64); and (e) $\gamma = 0.02$ (St = 0.98). The contour color range is from −2.0 to 2.0. The red color represents positive (counterclockwise) vorticity while the blue color represents negative (clockwise) vorticity. (For interpretation of the references to color in this figure legend, the reader is referred to the web version of this article.)

in Fig. 18(c) is termed as 2S-mode). After being convected further downstream, the two same-sign vortices coalesce and eventually the vortical structure similar to that in Fig. 18(c) is formed. This type of wake structure (2P-mode) has also been reported previously in [30]. At $\gamma = 0.08$, the symmetric vortex street which resembles the one in Fig. 18(c) is observed. At $\gamma = 0.02$, a deflected vortex street associated with the asymmetric flapping is observed. Compared with the one at $\gamma = \infty$, the direction of deflection of the vortex street has been switched. For this case, the backward-swimming mode is *not* observed. The non-periodic state can be reached if γ is further reduced.

For case C, the evolution of wake structure with decreasing bending rigidity is shown in Fig. 20. A symmetric wake is observed at $\gamma = \infty$ and $\gamma = 12.0$, while a deflected wake is observed at $\gamma = 5.0$ and $\gamma = 4.0$. At $\gamma = 0.4$, the backward-swimming mode is observed. The backward cruising velocity in this case is relatively larger than those in case A and case D (see Figs. 18(f) and 21(f) for comparisons). As a result, a symmetric vortex street (which resembles the one shown in Fig. 18(d)) is clearly seen behind the flapper.

Fig. 21 shows the wake structures at various bending rigidities in case D. At $\gamma = \infty$, a deflected vortex street is observed. At $\gamma = 2.4$, the up-down symmetry of the wake is preserved. At $\gamma = 1.2$, symmetry breaking occurs again in the wake and results in a deflected vortex street. It is also observed that the direction of deflection in the vortex street is now switched when compared with the one at $\gamma = \infty$. At $\gamma = 0.8$ the wake is also characterized by a deflected vortex street. It is interesting to see that the direction of deflection in the vortex street is switched again when compared with the one at $\gamma = 1.2$ (the direction of deflection is now the same as the one at

$\gamma = \infty$). Note in this study the initial condition is exactly the same for all simulations. This phenomenon has been reported previously in the studies of rigid flapping foils, both in experiment [47] and in simulation [48]. The reason for the switching of direction of the deflected wake at different bending rigidities is still not clear and merits further study. At $\gamma = 0.4$, the backward-swimming mode is also observed. The wake structure at this bending rigidity looks very similar to that of the backward-swimming mode in case A (see Fig. 18(f)). However, a very short vortex street can still be seen after careful examination. Due to the low cruising Reynolds number, the vortices shed into the wake decay very quickly.

By comparing the wake structures at $\gamma = \infty$ and at moderate bending rigidities in case B (or case D), it is conjectured that moderate flexibility can *inhibit* symmetry breaking of the wake. Further comments regarding the influence of flexibility on the stability property of the wake are presented here. As shown in Godoy-Diana et al. [49], the up-down symmetry of the reversed Karman vortex street can be persevered if the Strouhal number is less than a critical value (in the range of 0.33–0.44) for a *rigid* pitching foil at the Re number of 255. At the first glance, the ‘symmetry-preserving’ effect of flexibility can be attributed to reducing St number (to a value below the critical one). However, the observations of the current work cannot be simply rationalized by the fact that flexibility modifies the St number. It is found that for foils with moderate bending rigidities, the wake can stay symmetric at St number as high as 0.75 (see Fig. 18(d)), which is much higher than the critical Strouhal number for rigid foils. Another counterexample is shown in Fig. 21(b) and (c). At $\gamma = \infty$ and $\gamma = 2.4$, the St numbers are identical (which equal 0.39). The former one produces a deflected wake while the up-down symmetry is preserved in the latter one. We

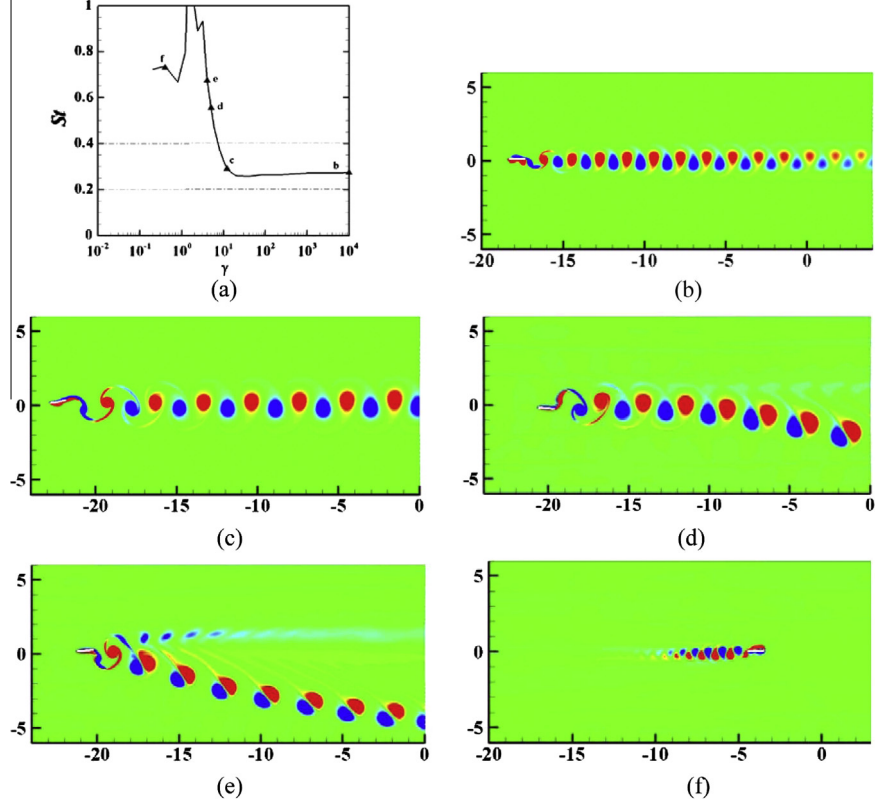


Fig. 20. Instantaneous vorticity contours for case C at various bending rigidities. St number as a function of bending rigidity is also plotted in (a) for reference purpose; (b) $\gamma = \infty$ ($\text{St} = 0.27$); (c) $\gamma = 12.0$ ($\text{St} = 0.29$); (d) $\gamma = 5.0$ ($\text{St} = 0.56$); (e) $\gamma = 4.0$ ($\text{St} = 0.68$); and (f) $\gamma = 0.4$ ($\text{St} = 0.73$). The contour color range is from -2.0 to 2.0 . The red color represents positive (counterclockwise) vorticity while the blue color represents negative (clockwise) vorticity. (For interpretation of the references to color in this figure legend, the reader is referred to the web version of this article.)

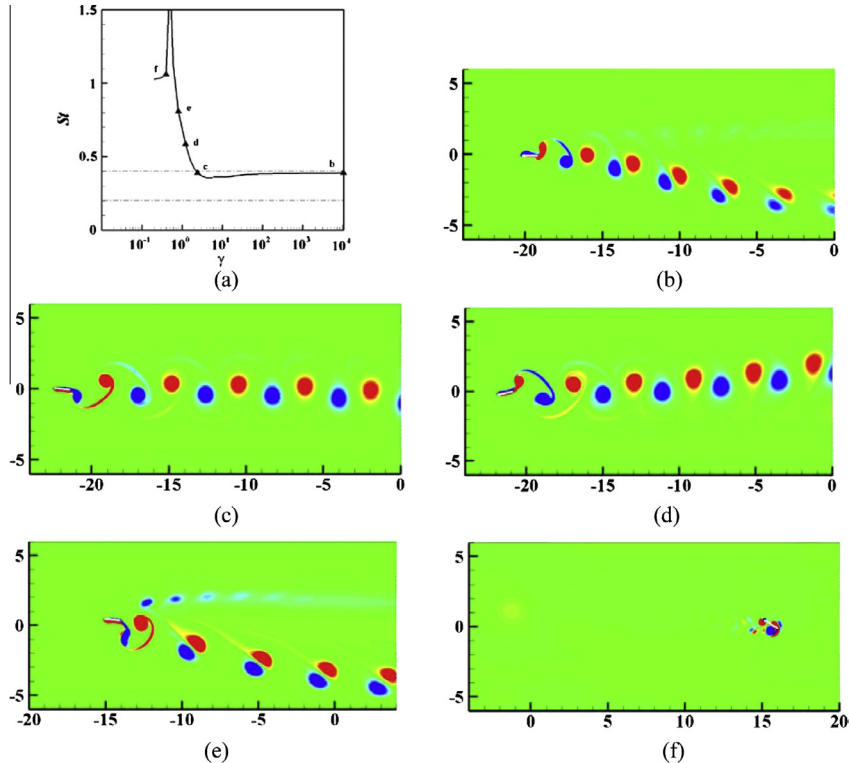


Fig. 21. Instantaneous vorticity contours for case D at various bending rigidities. St number as a function of bending rigidity is also plotted in (a) for reference purpose; (b) $\gamma = \infty$ ($\text{St} = 0.39$); (c) $\gamma = 2.4$ ($\text{St} = 0.39$); (d) $\gamma = 1.2$ ($\text{St} = 0.58$); (e) $\gamma = 0.8$ ($\text{St} = 0.81$); and (f) $\gamma = 0.4$ ($\text{St} = 1.06$). The contour color range is from -2.0 to 2.0 . The red color represents positive (counterclockwise) vorticity while the blue color represents negative (clockwise) vorticity. (For interpretation of the references to color in this figure legend, the reader is referred to the web version of this article.)

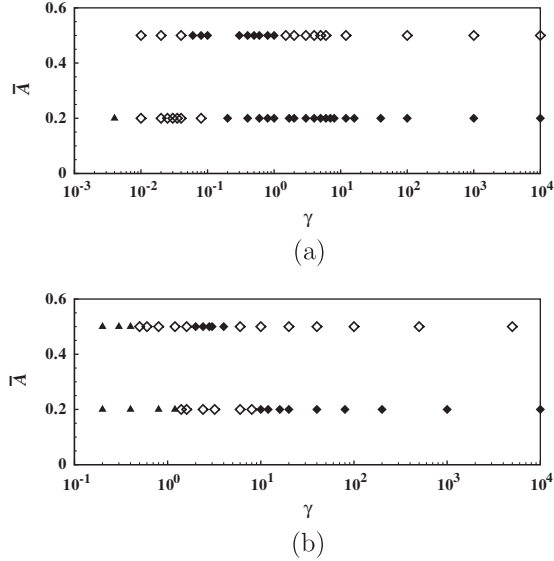


Fig. 22. A diagram map for the wake symmetry/asymmetry with respect to the bending rigidity and the plunging amplitude. (a) $\beta = 0.2$; (b) $\beta = 2.0$. The filled diamonds represent cases with symmetric wake in forward motion. The empty diamonds represent cases with asymmetric wake in forward motion. The filled triangles represent cases in backward motion.

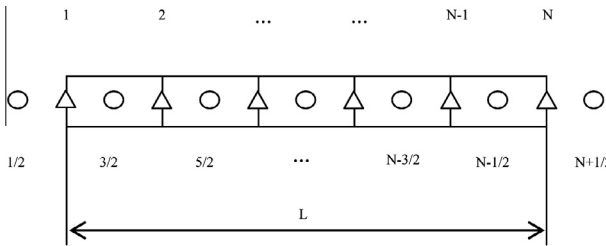


Fig. B1. The stencil used in the discretization of the structure equation. The displacement X is located at places denoted by triangles; while the tension coefficient is located at places denoted by circles.

notice that a similar observation was also reported in a more recent work by Marais et al. [50], where the symmetry breaking of the reversed Karman vortex street behind a flexible pitching foil has been *inhibited* in a large range of parameters explored. In another recent work by Zheng and Wei [51], it was observed that symmetry breaking of the wake behind a rigid plunging foil can be influenced *individually* by frequency and amplitude (even if the St number is kept fixed). Furthermore, they also found that symmetry breaking can also be affected by the (cruising) Reynolds number. The findings in these two papers can provide some clues for rationalizing the observations of the current work. In the current study, it is also observed that excessive flexibility can even trigger symmetry breaking in the wake (see Figs. 18(e) and 19(e)). To our knowledge, this is the first report of such phenomenon and the mechanism behind it is not well understood either. A diagram map for the wake symmetry/asymmetry with respect to the bending rigidity and the plunging amplitude are shown in Fig. 22. Further studies are needed to understand the mechanism for the transition of the wake (from symmetric pattern to asymmetric pattern or *visa versa*).

5. Conclusions

To investigate the influence of flexibility on the hydrodynamics of a self-propelled foil, we consider a simplified model problem in

which the two-dimensional laminar flow interacts with an inextensible filament. The control parameters in the model problem are: the flapping Reynolds number Re_f , the dimensionless oscillating amplitude \bar{A} , the mass ratio β and the dimensionless bending rigidity γ . In the numerical simulations, we fix the flapping Reynolds number to 200 and consider four different combinations of dimensionless oscillating amplitude and mass ratio. For each combination, we performed a series of simulations by varying the dimensionless bending rigidity in a certain range while keeping other parameters unchanged.

It is shown that for a specific plunging motion, the optimal cruising speed is always achieved in the foils with some passive flexibility and not the rigid ones. The bending rigidities for achieving the global maxima in cruising speed and propulsive parameter (which is used to characterize efficiency) are very close to each other. The range of reduced forcing frequency for achieving optimized performance lies much below the resonance point (0.52–0.64 for maximal cruising speed and 0.5–0.75 for maximal efficiency). Thus optimum performance cannot be achieved by seeking resonance. This numerical observation is consistent with the measurements of some flying insects, such as hoverfly and dragonfly. Rather than seeking resonance, we believe that the optimal propulsive performance is closely related to the ‘streamlined’ shape formed during flapping.

In the range of flexibility considered in this work, only mode shapes of mode-1 or mode-2 type are observed. In a certain range of bending rigidity, the up-down symmetry of the flapping motion can be lost (due to the occurrence of symmetry-breaking in the wake), although the plunging motion at the leading-edge is always perfectly symmetric. The dynamical states of the self-propelled foil can be classified into three types: non-periodic movement, periodic backward-movement and periodic forward-movement. The transition among these three states may occur with the increasing of bending rigidity. The periodic backward-movement state can be missing for specific parameter values.

The wake structures behind the self-propelled flapping foil in forward movement can be classified into two types: symmetric and deflected vortex streets. It is observed that moderate flexibility can inhibit symmetry breaking of the wake. Since a deflected vortex street is always associated with a net lift and torque, animals may avoid it when cruising. One important implication of this observation is that flexibility may be used favorably by animals during cruising, not only to achieve higher speed or efficiency but also to preserve wake symmetry. However, it is also observed that excessive flexibility can trigger symmetry breaking in the wake. Thus the effects of flexibility on the stability properties of the wake are very complex and still not well understood.

The results obtained in the current work shed some light on the role of flexibility in flapping-based biolocomotion. The model described in this paper can serve as a canonical problem for further numerical inquiries. There are several avenues for future research. Firstly, more thorough parametric studies, such as the effects of Re_f , \bar{A} and β , could be extremely helpful in assessing the overall performance of the system. Secondly, other kinematics, such as pitching or the combination of plunging and pitching needs to be studied. Thirdly, the influences of flexibility on the wake symmetry properties need to be further explored and this is one direction of our ongoing research.

Acknowledgements

This work is supported by Chinese Academy of Sciences under Project Nos. KJCX-SW-L08 and KJCX3-SYW-S01, National Natural Science Foundation of China under Project Nos. 10702074, 10872201, 11023001 and 11372331. The authors would like to thank Dr. Wei-Xi Huang for helpful discussions on the boundary

conditions used in the structure solver and the National Supercomputing Center in Tianjin (NSCC-TJ) for the allocation of computing time.

Appendix A. Dimensionless numbers used in this paper

Flapping Reynolds number: $\text{Re}_f = \frac{2\pi A_f L}{v} = \frac{U_{ref} L}{v}$;

Cruising Reynolds number: $\text{Re}_c = \frac{\tilde{U}_c L}{v} = \frac{U_{ref} L}{v} \cdot \frac{\tilde{U}_c}{U_{ref}} = U_c \cdot \text{Re}_f$;

Mass ratio: $\beta = \frac{\rho_s}{\rho_f}$;

Dimensionless bending rigidity: $\gamma = \frac{B}{\rho_f U_{ref}^2 L^3}$;

Dimensionless tension: $\zeta = \frac{T}{\rho_f U_{ref}^2 L}$;

Froude number: $Fr = \frac{gL}{U_{ref}^2}$;

Strouhal number: $St = \frac{2fA_T}{|U_c|} = \frac{1}{\pi} \frac{U_{ref}}{|U_c|} \frac{A_T}{A} = \frac{1}{\pi |U_c|} \frac{\bar{A}_T}{A}$;

Reduced forcing frequency: $\bar{\omega} = \frac{\omega_f}{\omega_1} = \frac{2\pi f}{\omega_1}$; with ω_1 being the first natural angular frequency.

Appendix B. Discretization of structural equation

The discretized form of Eq. (3) can be written as

$$\beta \frac{\mathbf{X}_i^{n+1} - 2\mathbf{X}_i^n + \mathbf{X}_i^{n-1}}{\Delta t^2} = (\mathbf{F}_t)_i^{n+1} + (\mathbf{F}_b)_i^{n+1} + \beta Fr \frac{\mathbf{g}}{g} - (\mathbf{F})_i^n, \quad (B1)$$

For X , $\begin{cases} i = 1, \dots, N \text{ (self-propelled)} \\ 2, \dots, N \text{ (pinned)} \end{cases}$

For Y , $i = 2, \dots, N$

where \mathbf{F}_t and \mathbf{F}_b are the tension force and bending force respectively. The superscripts $n-1$, n , and $n+1$ denote the indices of time steps, while the subscripts i denotes the index of node (see Fig. B1 for the stencil used in the discretization).

The tension force is computed by

$$(\mathbf{F}_t)_i^{n+1} = \frac{\zeta_{i+\frac{1}{2}}^{n+\frac{1}{2}} (D_s \mathbf{X}^{n+1})_{i+\frac{1}{2}} - \zeta_{i-\frac{1}{2}}^{n+\frac{1}{2}} (D_s \mathbf{X}^{n+1})_{i-\frac{1}{2}}}{\Delta s}, \quad i = 2, \dots, N-1,$$

$$(\mathbf{F}_t)_1^{n+1} = \frac{\zeta_{\frac{3}{2}}^{n+\frac{1}{2}} (D_s \mathbf{X}^{n+1})_{\frac{3}{2}}}{\Delta s}, \quad (\text{for self-propelled only})$$

$$(\mathbf{F}_t)_N^{n+1} = \frac{-\zeta_{N-\frac{1}{2}}^{n+\frac{1}{2}} (D_s \mathbf{X}^{n+1})_{N-\frac{1}{2}}}{\Delta s}, \quad (B2)$$

where D_s is the operator of first-order central difference defined as

$$(D_s \mathbf{X})_{i+\frac{1}{2}} = \frac{\mathbf{X}_{i+1} - \mathbf{X}_i}{\Delta s}, \quad (B3)$$

$$(D_s \mathbf{X})_{i-\frac{1}{2}} = \frac{\mathbf{X}_i - \mathbf{X}_{i-1}}{\Delta s}, \quad i = 2, \dots, N-1.$$

Note that in computing the tension force at end-points, the conditions $\zeta_{N+\frac{1}{2}}^{n+\frac{1}{2}} = 0$ and $\zeta_{\frac{1}{2}}^{n+\frac{1}{2}} = 0$ (for self-propelled foil only) are used in Eq. (B2).

The bending force is computed by

$$(\mathbf{F}_b)_i^{n+1} = -\gamma \frac{(D_{ss} \mathbf{X}^{n+1})_{i+1} - (D_{ss} \mathbf{X}^{n+1})_i + (D_{ss} \mathbf{X}^{n+1})_{i-1}}{\Delta s^2}, \quad i = 2, \dots, N-1,$$

$$(\mathbf{F}_b)_1^{n+1} = -\gamma \frac{(D_{sss} \mathbf{X}^{n+1})_{\frac{3}{2}} - (D_{sss} \mathbf{X}^{n+1})_{\frac{1}{2}}}{\Delta s} = -\gamma \frac{(D_{sss} \mathbf{X}^{n+1})_{\frac{3}{2}}}{\Delta s} \quad (\text{for self-propelled only}),$$

$$(\mathbf{F}_b)_N^{n+1} = -\gamma \frac{(D_{sss} \mathbf{X}^{n+1})_{N+\frac{1}{2}} - (D_{sss} \mathbf{X}^{n+1})_{N-\frac{1}{2}}}{\Delta s} = \gamma \frac{(D_{sss} \mathbf{X}^{n+1})_{N-\frac{1}{2}}}{\Delta s}, \quad (B4)$$

where D_{ss} is the operator of second-order central difference defined as

$$(D_{ss} \mathbf{X})_i = \frac{(D_s \mathbf{X})_{i+\frac{1}{2}} - (D_s \mathbf{X})_{i-\frac{1}{2}}}{\Delta s}, \quad i = 1, \dots, N-1,$$

$$(D_{ss} \mathbf{X})_N = (0, 0).$$

In Eq. (B4), D_{sss} is the operator of third-order difference defined as

$$(D_{sss} \mathbf{X})_{\frac{3}{2}} = \frac{(D_{ss} \mathbf{X})_2 - (D_{ss} \mathbf{X})_1}{\Delta s} \quad (\text{for pinned})$$

$$(D_{sss} \mathbf{X})_{\frac{3}{2}} = \frac{(D_{ss} \mathbf{X})_2 - [(D_s \mathbf{X})_{\frac{3}{2}} - (1, 0)]}{\Delta s} \quad (\text{for self-propelled})$$

$$(D_{sss} \mathbf{X})_{N-\frac{1}{2}} = \frac{(D_{ss} \mathbf{X})_N - (D_{ss} \mathbf{X})_{N-1}}{\Delta s} = \frac{-(D_{ss} \mathbf{X})_{N-1}}{\Delta s}. \quad (B6)$$

The computation of $(F_b^{(2)})_1$ in the case of self-propelled foil will be described later.

The discretized form of Eq. (6) can be written as

$$(D_s \mathbf{X}^*)_{i+\frac{1}{2}} \cdot [D_s (D_s (\zeta^{n+1/2} D_s \mathbf{X}^*))]_{i+\frac{1}{2}}$$

$$= \frac{1}{2} D_t^+ D_t^- (D_s \mathbf{X}^n \cdot D_s \mathbf{X}^n)_{i+\frac{1}{2}} - (D_s \mathbf{U}^n \cdot D_s \mathbf{U}^n)_{i+\frac{1}{2}}$$

$$- (D_s \mathbf{X}^*)_{i+\frac{1}{2}} \cdot [D_s (\mathbf{F}_b^* - \mathbf{F}^n)]_{i+\frac{1}{2}}, \quad i = 1, 2, \dots, N-1, \quad (B7)$$

where \mathbf{X}^* is the predicted displacement vector for the Lagrangian point at time step $n+1$ by using a temporal extrapolation from those at time steps $n-1$ and n , i.e., $\mathbf{X}^* = 2\mathbf{X}^n - \mathbf{X}^{n-1}$. \mathbf{F}_b^* is the bending force evaluated at \mathbf{X}^* . D_t^+ and D_t^- are the first order forward and backward difference operator in time respectively.

For the self-propelled foil, a supplementary relation is needed for computing $F_b^{(2)}$ (or $F_b^{(2)}$) at the leading-edge in Eq. (B7) (or Eq. (B4)). This relation can be derived by using $(\frac{\partial^2 Y^*}{\partial t^2})_1 = \ddot{y}(t)$ or $(F_t^{*(2)})_1 + (F_b^{*(2)})_1 - (F^{(2)})_1 + \beta Fr \frac{g^{(2)}}{g} = \ddot{y}(t)$. Since $(F_t^{*(2)})_1 = 0$, it now becomes $(F_b^{*(2)})_1 = (F^{(2)})_1 - \beta Fr \frac{g^{(2)}}{g} + \ddot{y}(t)$.

For the filament with a pinned leading-edge, in addition to Eq. (12), one more boundary condition of ζ is needed for solving Eq. (B7). This supplementary relation (between $\zeta_{\frac{1}{2}}$ and $\zeta_{\frac{3}{2}}$) can be derived by using the condition $(\frac{\partial^2 \mathbf{X}}{\partial t^2})_1 = 0$ (or $(\mathbf{F}_t)_1 + (\mathbf{F}_b)_1 - (\mathbf{F}_1)_1 + \beta Fr \frac{\mathbf{g}}{g} = 0$). Substituting Eqs. (B2) and (B4), this condition becomes

$$[D_s (\zeta D_s \mathbf{X})]_1 - [D_{ss} (\gamma D_{ss} \mathbf{X})]_1 = (\mathbf{F})_1 - \beta Fr \frac{\mathbf{g}}{g}. \quad (B8)$$

References

- [1] Ho S, Nassef H, Pornsinsirikar N, Tai YC, Ho CM. Unsteady aerodynamics and flow control for flapping wing flyers. *Prog Aerosp Sci* 2003;39:635–81.
- [2] Shyy W, Lian Y, Tang J, Liu H, Trizila P, Standford B, et al. Computational aerodynamics of low Reynolds number plunging, pitching and flexible wings for MAV applications. *Acta Mech Sin* 2008;24:351–73.
- [3] Daniel TL, Combes SA. Flexible wings and fins: bending by inertial or fluid-dynamic forces? *Integr Compar Biol* 2002;42:1044–9.
- [4] Heathcote S, Martin D, Gursul I. Flexible flapping airfoil propulsion at zero freestream velocity. *AIAA J* 2004;42:2196–204.
- [5] Heathcote S, Gursul I. Flexible flapping aerofoil propulsion at low Reynolds numbers. *AIAA J* 2007;45:1066–79.
- [6] Heathcote S, Wang Z, Gursul I. Effect of spanwise flexibility on flapping wing propulsion. *J Fluids Struct* 2008;24:183–99.
- [7] Ishihara D, Yamashita Y, Horie T, Yoshida S, Niho T. Passive maintenance of high angle of attack and its lift generation during flapping translation in crane fly wing. *J Exp Biol* 2009;212:3882–91.
- [8] Zhao L, Huang Q, Deng X, Xane SP. Aerodynamic effects of flexibility in flapping wings. *J R Soc Interf* 2010;44:485–97.
- [9] Katz J, Weihs D. Hydrodynamic propulsion by large amplitude oscillation of an airfoil with chordwise flexibility. *J Fluid Mech* 1978;88:713–23.
- [10] Michelin SB, Llewellyn Smith SG. Resonance and propulsion performance of a heaving flexible wing. *Phys Fluids* 2009;21:071902.

- [11] Vanella M, Fitzgerald T, Preidikman S, Balaras E, Balachandran B. Influence of flexibility on the aerodynamic performance of a hovering wing. *J Exp Biol* 2009;212:95–105.
- [12] Ishihara D, Horie T, Denda M. A two-dimensional computational study on the fluid–structure interaction cause of wing pitch changes in dipteran flapping flight. *J Exp Biol* 2009;212:1–10.
- [13] Eldredge JD, Toomey J, Medina A. On the roles of chord-wise flexibility in a flapping wing with hovering kinematics. *J Fluid Mech* 2010;659:94–115.
- [14] Chimakurthi SK, Tang J, Palacios R, Cesnik CES, Shyy W. Computational aeroelasticity framework for analyzing flapping wing micro air vehicles. *AIAA J* 2009;47:1865–78.
- [15] Kang CK, Aono H, Cesnik CES, Shyy W. Effects of flexibility on the aerodynamic performance of flapping wings. *J Fluid Mech* 2011;689:32–74.
- [16] Albuquerque DMS, Pereira JMC, Pereira JCF. Calculation of a deformable membrane airfoil in hovering flight. *CMES – Comput Model Eng* 2011;72:337–66.
- [17] Nakata T, Liu H. A fluid–structure interaction model of insect flight with flexible wings. *J Comput Phys* 2012;231:1822–47.
- [18] Nakata T, Liu H. Aerodynamic performance of a hovering hawkmoth with flexible wings: a computational approach. *Proc R Soc B* 2012;279:722–31.
- [19] Yin B, Luo H. Effect of wing inertia on hovering performance of flexible flapping wings. *Phys Fluids* 2010;22:111902.
- [20] Ferreira de Sousa PJSA, Allen JJ. Thrust efficiency of harmonically oscillating flexible flat plates. *J Fluid Mech* 2011;674:43–66.
- [21] Masoud H, Alexeev A. Resonance of flexible flapping wings at low Reynolds number. *Phys Rev E* 2010;81:056304.
- [22] Qi D, Liu Y, Shyy W, Aono H. Simulations of dynamics of plunge and pitch of a three-dimensional flexible wing in a low Reynolds number flow. *Phys Fluids* 2010;22:091901.
- [23] Lauder GV, Anderson EJ, Tangorra J, Madden PG. Fish biorobotics: kinematics and hydrodynamics of self-propulsion. *J Exp Biol* 2007;210:2767–80.
- [24] Vandenberghe N, Zhang J, Childress S. Symmetry breaking leads to forward flapping flight. *J Fluid Mech* 2004;506:147–55.
- [25] Vandenberghe N, Childress S, Zhang J. On unidirectional flight of a free flapping wing. *Phys Fluids* 2006;18:014102.
- [26] Alben S, Shelley M. Coherent locomotion as an attracting state for a free flapping body. *Proc Natl Acad Sci USA* 2005;102:11163–6.
- [27] Lu XY, Liao Q. Dynamic responses of a two-dimensional flapping foil motion. *Phys Fluids* 2006;18:098104.
- [28] Zhang X, Ni S, Wang SZ, He GW. Effects of geometric shape on the hydrodynamics of a self-propelled flapping foil. *Phys Fluids* 2009;21:103302.
- [29] Spagnolie SE, Moret L, Shelley MJ, Zhang J. Surprising behaviors in flapping locomotion with passive pitching. *Phys Fluids* 2010;22:041903.
- [30] Zhang J, Liu NS, Lu XY. Locomotion of a passively flapping flat plate. *J Fluid Mech* 2010;659:43–68.
- [31] Eldredge JD, Pisani D. Passive locomotion of a simple articulated fish-like system in the wake of an obstacle. *J Fluid Mech* 2008;607:279–88.
- [32] Wilson MM, Eldredge JD. Performance improvement through passive mechanics in jellyfish-inspired swimming. *Int J Nonlin Mech* 2011;46:557–67.
- [33] Thiria B, Godoy-Diana R. How wing compliance drives the efficiency of self-propelled flapping flyers. *Phys Rev E* 2010;82:015303(R).
- [34] Ramananarivo S, Godoy-Diana R, Thiria B. Rather than resonance, flapping wing flyers may play on aerodynamics to improve performance. *Proc Natl Acad Sci USA* 2011;108:5964–9.
- [35] Alben S, Witt C, Baker TV, Anderson E, Lauder GV. Dynamics of freely swimming flexible foils. *Phys Fluids* 2012;24:051901.
- [36] Lee J, Lee S. Fluid–structure interaction for the propulsive velocity of a flapping flexible plate at low Reynolds number. *Comput Fluids* 2013;71:348–74.
- [37] Zhu L, Peskin CS. Simulation of a flapping flexible filament in a flowing soap film by the immersed boundary method. *J Comput Phys* 2002;179:452–68.
- [38] Connell BSH, Yue DKP. Flapping dynamics of a flag in a uniform stream. *J Fluid Mech* 2007;581:33–67.
- [39] Huang WX, Shin SJ, Sung HJ. Simulation of flexible filaments in a uniform flow by the immersed boundary method. *J Comput Phys* 2007;226:2206–28.
- [40] Wang S, Zhang X. An immersed boundary method based on discrete stream function formulation for two- and three-dimensional incompressible flows. *J Comput Phys* 2011;230:3479–99.
- [41] Borazjani I, Sotiropoulos F. Numerical investigation of the hydrodynamics of carangiform swimming in the transitional and inertial flow regimes. *J Exp Biol* 2008;211:1541–58.
- [42] Kern S, Koumoutsakos P. Simulations of optimized anguilliform swimming. *J Exp Biol* 2006;209:4841–57.
- [43] Tanaka H, Whitney JP, Wood RJ. Effect of flexural and torsional wing flexibility on lift generation in hoverfly flight. *Integr Comput Biol* 2011;51:142–50.
- [44] Combes SA, Daniel TL. Flexural stiffness in insect wings II. Spatial distribution and dynamic wing bending. *J Exp Biol* 2003;206:2989–97.
- [45] Anderson JM, Streitlien K, Barrett DS, Triantafyllou MS. Oscillating foils of high propulsive efficiency. *J Fluid Mech* 1998;360:41–72.
- [46] Taylor GK, Nudds RL, Thomas ALR. Flying and swimming animals cruise at a Strouhal number tuned for high power efficiency. *Nature* 2003;425:707–11.
- [47] Heathcote S, Gursul I. Jet switching phenomenon for a periodically plunging airfoil. *Phys Fluids* 2007;19:027104.
- [48] Lewin GC, Haj-Hariri H. Modeling thrust generation of a two-dimensional heaving airfoil in a viscous flow. *J Fluid Mech* 2003;492:339–62.
- [49] Godoy-Diana R, Aider JL, Wesfreid JE. Transitions in the wake of a flapping foil. *Phys Rev E* 2008;77:016308.
- [50] Marais C, Thiria B, Wesfreid JE, Godoy-Diana R. Stabilizing effect of flexibility in the wake of a flapping foil. *J Fluid Mech* 2012;710:659–69.
- [51] Zheng ZC, Wei Z. Study of mechanisms and factors that influence the formation of vortical wake of a heaving airfoil. *Phys Fluids* 2012;24:103601.
- [52] Dai H, Luo HX, Doyle JF. Dynamic pitching of an elastic rectangular wing in hovering motion. *J Fluid Mech* 2012;693:473–99.
- [53] Dai H, Luo HX, Ferreira de Sousa PJSA, Doyle JF. Thrust performance of a flexible low-aspect-ratio pitching plate. *Phys Fluids* 2012;24:101903.